Thin Solid Films 834 (2026) 140852

Contents lists available at ScienceDirect

Thin Solid Films

journal homepage: www.elsevier.com/locate/tsf

Synthesis of Graphene on catalyst copper substrates: Growth mechanisms and friction behavior

M.F.C. Ordoñez [a,b,*], D.J. Feria [c], I. Pereyra [c], M.N.P. Carreño [c], R.M. Souza [b], A.P. Tschiptschin [a]

[a] Metallurgical and Materials Engineering Department, University of São Paulo, Av. Professor Mello Moraes, 2463, SP 0550-030, Brazil
[b] Surface Phenomena Laboratory, Polytechnic School, University of São Paulo, Av. Prof. Mello Moraes, 2231, SP 05508-030, Brazil
[c] Center for Electrical Engineering, Polytechnic School, University of Sao Paulo, Av. Prof. Luciano Gualberto, 158, SP 05508-010, Brazil

ARTICLE INFO

Keywords:
Graphene
Copper
Thermal annealing
Tribology
Atomic force microscopy friction mapping
Macroscale wear
Wear
Raman spectroscopy

ABSTRACT

This work investigates the synthesis, characterization, and tribological performance of bi- and few-layer graphene using copper substrates as catalysts. Two types of copper substrates were employed: bulk copper foils (0.25 mm thickness) and thin copper films (~800 nm thickness) deposited by magnetron sputtering. Bilayer amorphous-carbon/copper (a-C/Cu) and copper/amorphous-carbon (Cu/a-C) films were also produced as solid-carbon-source substrates. Graphene formation occurred via two distinct thermal processes: (1) catalytic chemical vapor deposition (CVD) on bulk copper foils and on copper films without amorphous carbon, using methane as the carbon precursor under Ar–H_2 atmospheres; and (2) annealing of a-C/Cu and Cu/a-C films under H_2–Ar without methane, in which graphene forms by carbon diffusion from the solid source. Raman spectroscopy confirmed the presence of bi- and few-layer graphene, revealing variations in layer number, crystallinity, and structural disorder. Atomic force microscopy (AFM) lateral-friction mapping showed local friction reduction in graphene-covered regions, confirming its role in modulating nanoscale tribological response. Macroscale sliding tests under normal loads of 0.5–2 N revealed load-dependent behavior: the lowest load yielded a stable low friction coefficient (~0.18), whereas higher loads increased friction (up to 0.35) and wear rates due to progressive graphene removal. Raman analysis of the worn tracks showed loss of the 2D band, increased D-band intensity, and the emergence of D + G features, indicating disorder, amorphization, and partial oxidation of the exposed copper substrate. The results demonstrate that although graphene initially reduces friction and protects the surface, prolonged load-bearing contact is governed by the stability of its ultrathin layers.

1. Introduction

Graphene is a two-dimensional carbon allotrope with atoms arranged in a honeycomb lattice, exhibiting exceptional electrical, mechanical, and optical properties that have stimulated extensive research since its first isolation [1,2]. Its unique characteristics make it highly promising for a wide range of applications, including flexible electronics, energy storage, sensors, and tribological coatings. Consequently, a variety of synthesis strategies have been developed to produce high-quality graphene films on different substrates.

Chemical vapor deposition (CVD) has emerged as one of the most effective and scalable routes for graphene synthesis, particularly when using transition metals as catalysts. Nickel and copper are among the most widely employed substrates, although they exhibit distinct catalytic behaviors. In nickel, carbon atoms dissolve at high temperatures and segregate upon cooling, often resulting in multilayer graphene [3,4]. In contrast, due to the low solubility of carbon in copper, graphene growth is dominated by surface adsorption, favoring the formation of monolayers [5]. These differences highlight the crucial role of the catalytic substrate in governing nucleation density, growth kinetics, and film morphology.

Several studies have examined the influence of growth parameters and substrate morphology on graphene quality. Han et al. [6] demonstrated that copper surface roughness, grain boundaries, and impurities act as preferential nucleation sites, directly impacting the density and size of graphene domains. Similarly, Vlassiouk et al. [7] showed that hydrogen plays a dual role during CVD growth of graphene on copper, activating the surface while simultaneously etching graphene, thus

* Corresponding author at: Metallurgical and Materials Engineering Department, University of São Paulo, Av. Professor Mello Moraes, 2463, SP 0550-030, Brazil.
E-mail address: michaelfkn@alumni.usp.br (M.F.C. Ordoñez).

https://doi.org/10.1016/j.tsf.2026.140852
Received 30 August 2025; Received in revised form 30 December 2025; Accepted 2 January 2026
Available online 3 January 2026

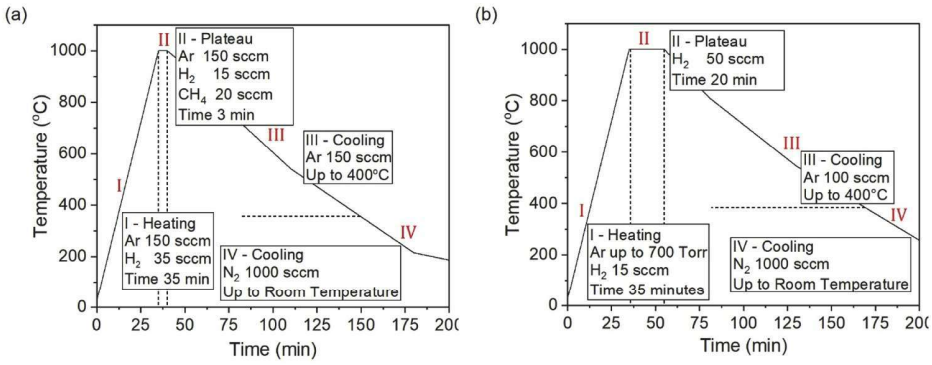

Fig. 1. Thermal cycle performed by the CVD method for (a) the copper foils, and for the copper films using methane precursor, and (b) for the a-C/Cu and Cu/a-C films using amorphous solid carbon precursor.

Table 1
Deposition parameters for Cu and amorphous carbon films under P1 and P2 sputtering conditions.

Parameters	P (W)		P_B (Pa)	P_T (Pa)	Ar flow (sccm)	Bias (V)	T (min)	
	Cu	C					Cu	C
P1	50	300	2.67×10^{-2}	2.67×10^{-1}	10	−50	30	6
P2	170	300	1.33×10^{-3}	9.33×10^{-2}	15	−50	10.5	6

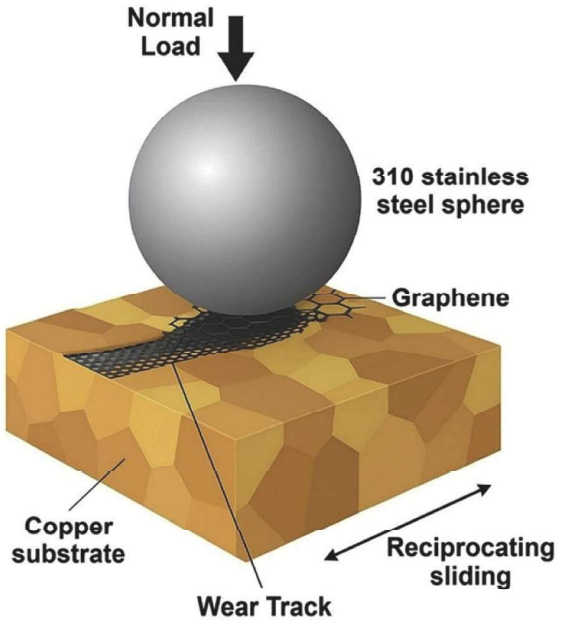

Fig. 2. Schematic representation of the friction test between copper-graphene foils and a 6 mm diameter 310 steel ball, in a ball-on-disk configuration.

influencing nucleation, growth rate, and the number of layers. Together, these findings emphasize the interplay between substrate conditions and gas-phase chemistry in determining the graphene structure.

Alternative synthesis strategies have also been proposed to bypass the need for hydrocarbon gas precursors. Hofrichter et al. [4] reported the use of amorphous SiC as a solid carbon source with nickel as a solvent layer, enabling graphene formation on insulating SiO_2/Si substrates after metal removal. Vishwakarma et al. [8] further extended this concept by growing graphene directly from amorphous carbon films using a Sn catalyst on SiO_2/Si, achieving transfer-free deposition at relatively low temperature (250 °C). These approaches illustrate the versatility of solid-state carbon sources for graphene growth, expanding the range of accessible substrates and processing conditions.

Beyond synthesis, characterization techniques are essential to evaluate graphene quality. Raman spectroscopy is the most widely used tool, providing information on the number of layers, stacking order, crystallinity, and defect density. The G and 2D bands, as well as the defect-activated D band, serve as fingerprints to assess structural quality and disorder [9,10]. Complementary techniques such as scanning electron microscopy (SEM) and atomic force microscopy (AFM) provide morphological insights, including surface roughness, voids, and island formation, which are critical to understanding growth mechanisms and film uniformity. AFM, in particular, allows nanoscale probing of frictional properties, making it a valuable tool to correlate local tribological behavior with graphene coverage and continuity [11,12].

In addition to structural and morphological evaluation, graphene's outstanding properties have motivated investigations into its tribological performance. Graphene films can act as solid lubricants by reducing friction and wear at sliding interfaces, functioning as protective and lubricating layers [13,14]. Recent reviews emphasize that graphene and related materials, including graphene oxide, reduced graphene oxide, and functionalized derivatives, exhibit remarkable lubrication capabilities. However, their effectiveness depends strongly on factors such as adhesion to the substrate, defect density, and environmental conditions [15]. While superlubricity can be achieved at the nanoscale, challenges remain at the macroscale, where poor interfacial adhesion and instability in lubricating environments limit the performance. These findings underscore the importance of linking growth conditions, structural integrity, and tribological behavior to perform practical applications of graphene coatings and lubricants.

This work investigates the synthesis of graphene on copper substrates using both gaseous (methane) and solid (amorphous carbon) precursors via CVD, supported by structural and morphological characterization through Raman spectroscopy, field-emission scanning electron microscopy (FE-SEM), and atomic force microscopy (AFM). In addition to comparing how precursor type and growth conditions affect graphene formation, exploratory tribological tests were performed to evaluate the functional response of the resulting films. Importantly, this study also highlights how local variations in graphene morphology, revealed through AFM lateral-friction mapping and Raman analysis, influence friction at the microscale. By establishing this connection between microstructure and tribological behavior, the work provides

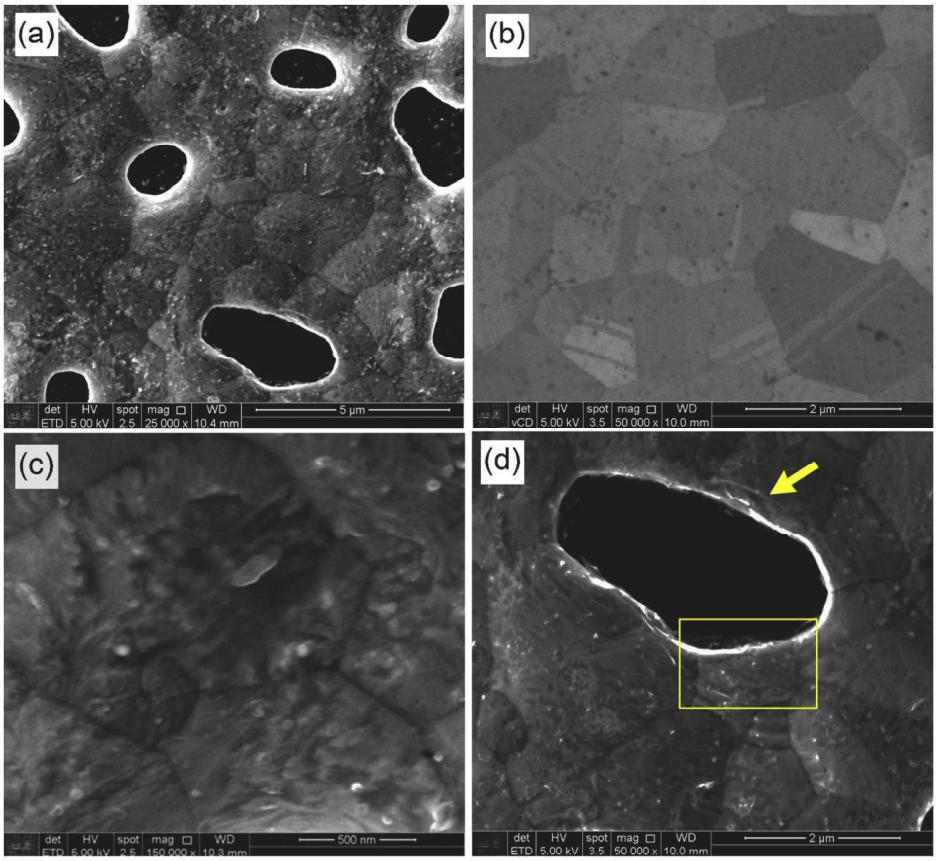

Fig. 3. SEM images of Cu films after 5 min of annealing at 1000 °C: (a) copper grain boundaries and holes formed due to film removal, (b) presence of contamination, (c) grains exhibiting graphene growth, and (d) hole boundaries highlighting the graphene layer (indicated by the rectangle and the yellow arrow).

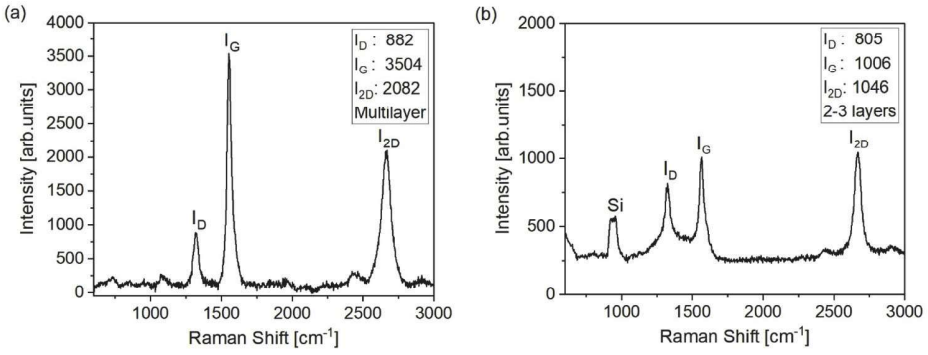

Fig. 4. Raman spectra from Cu films after graphene growth using methane (CH_4) as the carbon source. (a) Regions showing multilayer graphene, and (b) regions where graphene consists of 2–3 layers.

complementary insight into the mechanisms governing graphene's lubricating performance, contributing to the broader understanding of how synthesis routes impact both structural quality and functional properties.

2. Experimental procedure

Graphene synthesis was performed using a metallic catalyst with two different carbon precursors, a gaseous hydrocarbon (methane) and solid amorphous carbon, followed by thermal annealing. Initially, the preparation of the metallic catalyst in bulk (foils) and thin film form is described. Subsequently, the deposition conditions of the thin films are detailed. Thermal cycles for graphene formation are presented for each type of carbon precursor (Fig. 1). Finally, characterization techniques used to analyze the surface microstructure and chemical composition of graphene are described.

2.1. Preparation of the metallic catalyst

Copper was selected as the main catalyst due to its low carbon solubility, which favors self-limited graphene growth with few layers. The catalyst was provided both as micrometer-thick bulk foils and nanometer-thick thin films. Surface roughness, defects, and film thickness were considered as factors affecting graphene formation. Oxygen-free high thermal conductivity (OFHC) copper foils of 0.25 mm thickness were cut into 30 mm diameter discs. Both faces were ground, and

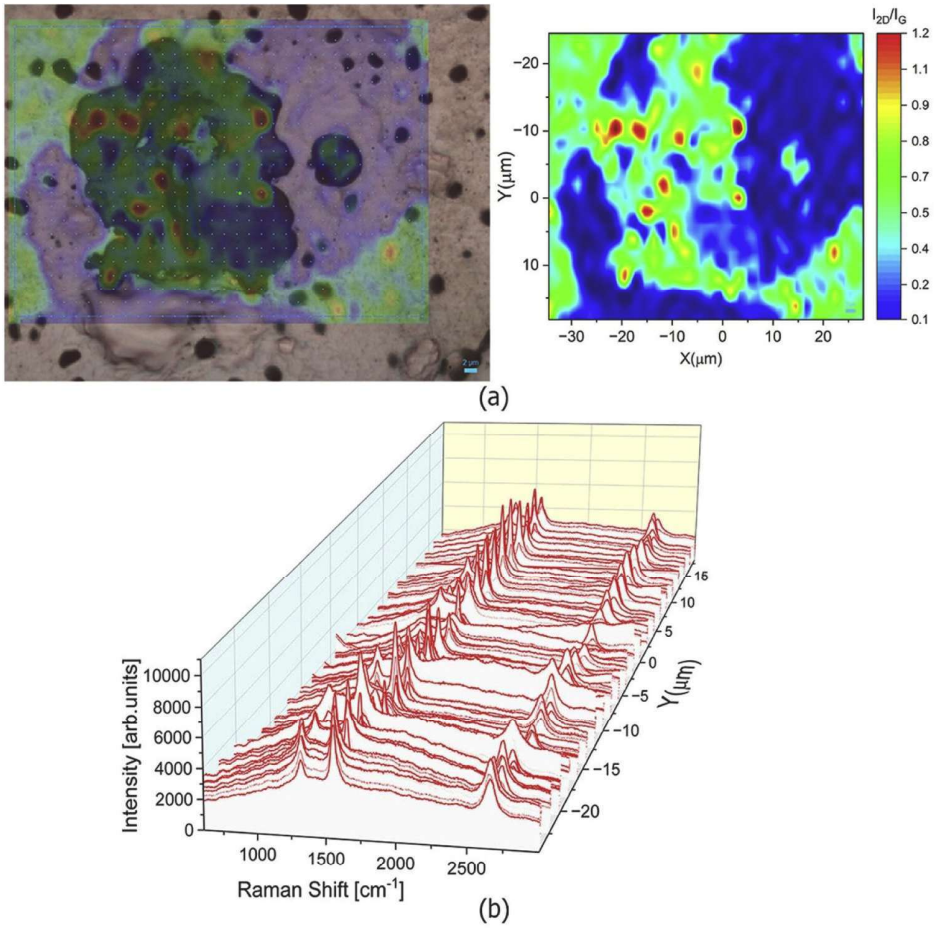

Fig. 5. Raman mapping of the Cu film surface after treatment: (a) intensity ratio I_{2D}/I_G, and (b) spectra obtained from a data row used to construct the map.

one face was polished up to 1 μm diamond paste. Immersion in glacial acetic acid for 5 min removed residual oxides. Finally, the samples were rinsed in acetone and isopropanol for 10 min.

Copper and amorphous carbon thin films were deposited by pulsed DC magnetron sputtering. Two sets of deposition parameters were employed to assess their effect on copper oxidation and film properties (Table 1). Parameter set P1 used lower power and higher working pressure, resulting in more oxidation, while set P2 employed higher power and lower pressure to minimize oxidation. Based on thickness measurements obtained by profilometry, the Cu deposition rate for both P1 and P2 conditions was determined to be 76 ± 2 nm/min. Copper films with final thicknesses of 400 nm and 800 nm were deposited by adjusting the deposition time accordingly. All films were deposited on Si (100) and on thermally oxidized SiO_2/Si substrates with a 300 nm oxide layer.

2.2. Thermal treatment

The CVD growth was performed in a hot-wall quartz tube furnace (5-inch diameter) equipped with vacuum control and mass-flow-regulated gas inlets. Prior to growth, the Cu foils and Cu thin films were loaded into the quartz tube and the system was purged with argon and evacuated under moderate vacuum (three purge–vacuum cycles), followed by evacuation to high vacuum (~3.3×10^{-1} Pa). After this step, ultrapure Ar was introduced to bring the system back to atmospheric pressure.

During the heating stage up to 950–1000 °C, the samples were maintained under a constant argon flow of 150 sccm. The heating rate to reach the annealing temperature was approximately 25–30 °C/min. For the growth using methane as gaseous precursor, corresponding to the thermal cycle shown in Fig. 1(a), hydrogen (15 sccm) and methane (20 sccm) were introduced after reaching the target temperature, resulting in an H_2/CH_4 flow ratio of 0.75. All experiments in this route were performed under an argon carrier atmosphere at near-atmospheric pressure. Plateau times of 3 and 15 min were used to evaluate graphene nucleation density and domain evolution on the Cu surface, with hydrogen acting as a co-catalyst during methane dehydrogenation.

For the growth using solid amorphous carbon precursor, corresponding to Fig. 1(b), Cu/a-C and a-C/Cu stacks were annealed in the same temperature range to induce the crystallization of amorphous carbon into graphene. In this route, no methane was used; therefore, no H_2/CH_4 ratio applies. The number of layers was controlled by the a-C thickness, while hydrogen promoted carbon activation and the selective removal of excess disordered carbon.

After the growth stage, methane and hydrogen flows (when applicable) were shut off, and the samples were cooled rapidly from 1000 °C to 400 °C under 100 sccm of Ar. Below 400 °C, cooling proceeded slowly to room temperature under a constant flow of high-purity nitrogen (1000 sccm), minimizing oxidation and preserving graphene quality.

2.3. Characterization

The microstructure of bulk copper, thin films, and formed graphene was examined by field-emission scanning electron microscopy (FE-SEM, FEI Inspect 50) coupled with energy-dispersive X-ray spectroscopy (EDS). SEM images were acquired using acceleration voltages of 20 kV for general microstructural examination and 5 kV for improved

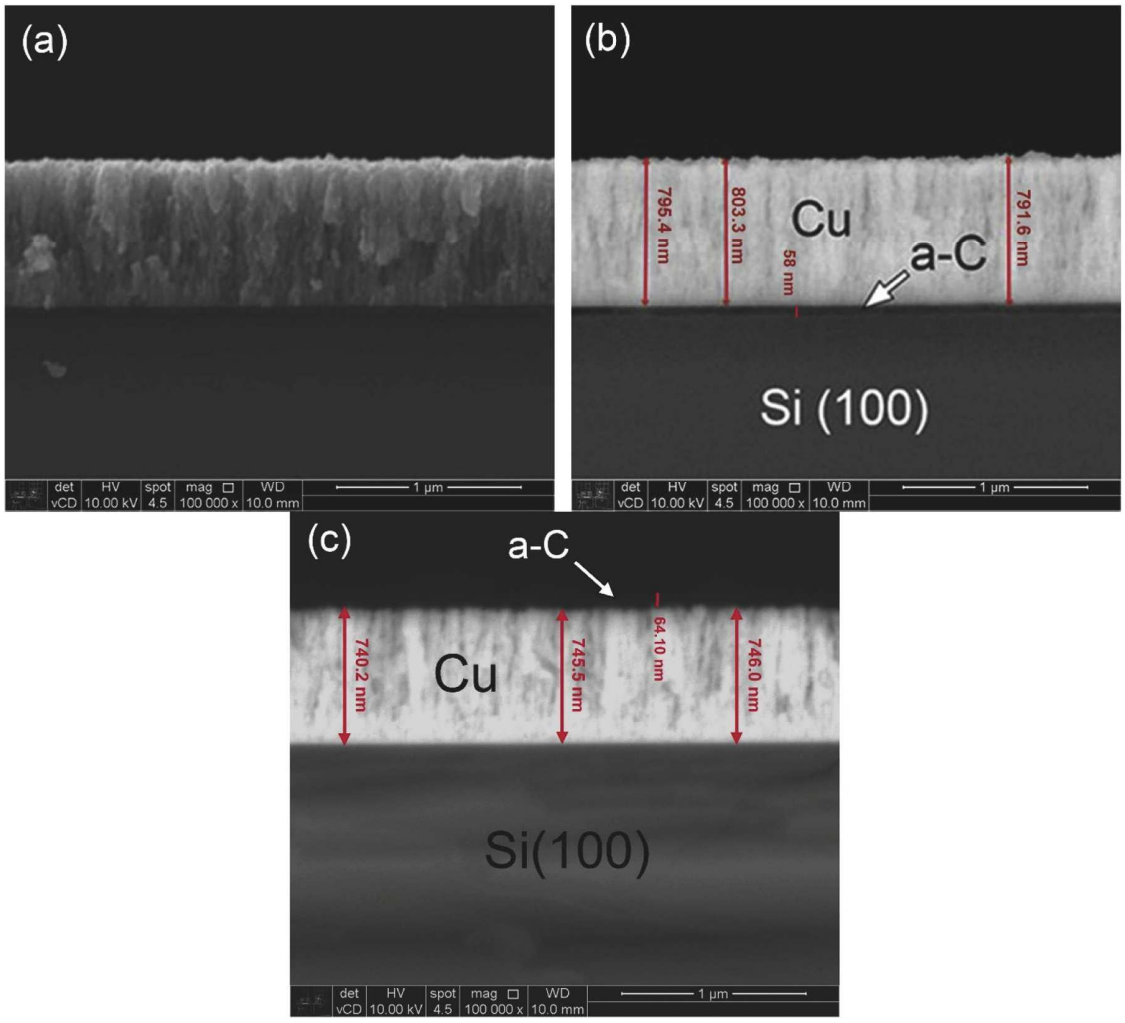

Fig. 6. SEM images of the cross-section of films deposited by Magnetron Sputtering with amorphous carbon on Si substrates (a) and (b) Cu / a-C film, and (c) a-C / Cu film.

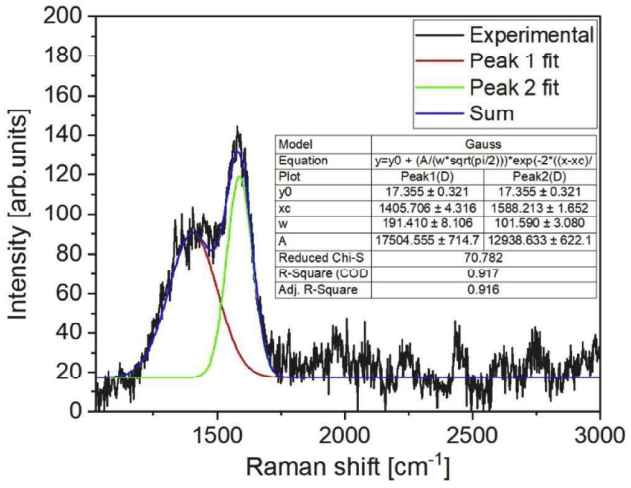

Fig. 7. Raman spectrum of the a-C (~40 nm) / Cu film deposited by PVD Magnetron Sputtering.

graphene contrast, with a working distance of approximately 10 mm. Graphene formation was analyzed using Raman spectroscopy (Xplora, Horiba) with a 532 nm laser and 20–25 mW power. Raman maps (34 × 22 points, 2 µm spacing) were generated to assess homogeneity and number of layers.

2.3.1. *Atomic force microscopy (AFM)*

AFM analyses were performed in ambient air using a Multimode 8 (Bruker) system. Images were acquired in tapping mode with sharp silicon tips (~15 nm radius) and cantilevers with ~250 kHz resonance frequency. Topography and qualitative local friction variations between graphene-covered and bare copper regions were evaluated. Contact mode with simultaneous lateral friction acquisition ("friction loop") was also employed. The cantilever spring constant was determined by thermal tuning (k = 0.1682 N/m) and vertical sensitivity was ~42.1 nm/V. Following Marsden et al. [16], lateral signals were processed qualitatively by subtracting trace and retrace scans to eliminate topography effects, generating friction contrast maps highlighting relatively high- and low-friction regions.

2.3.2. *Tribological behavior*

Friction and wear behavior of the copper-graphene foils (annealed for 15 min) were studied using a ball-on-disk tribometer (UMT-5, Bruker) in a reciprocating test against a 6 mm diameter 310 stainless steel ball. The disk was moved at an average sliding speed of 0.003 m/s with a stroke length of 8 mm, under different applied normal loads of

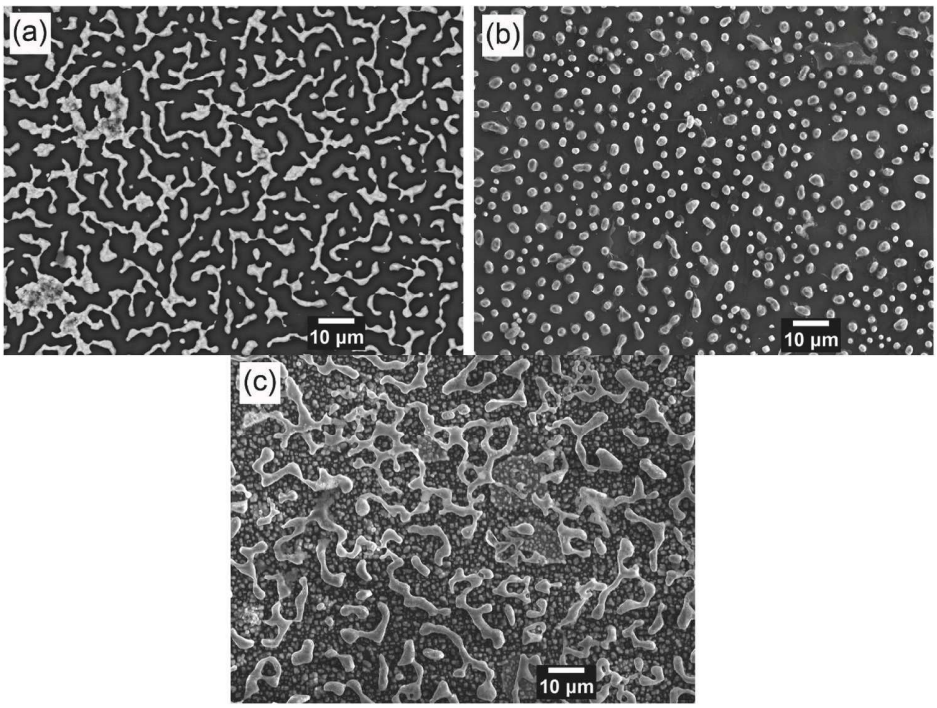

Fig. 8. Effect of treatment temperature and thickness of Cu / a-C / Si films on surface morphology: (a) 400 nm films at 950 °C, (b) 400 nm films at 1000 °C, and (c) 800 nm film at 1000 °C.

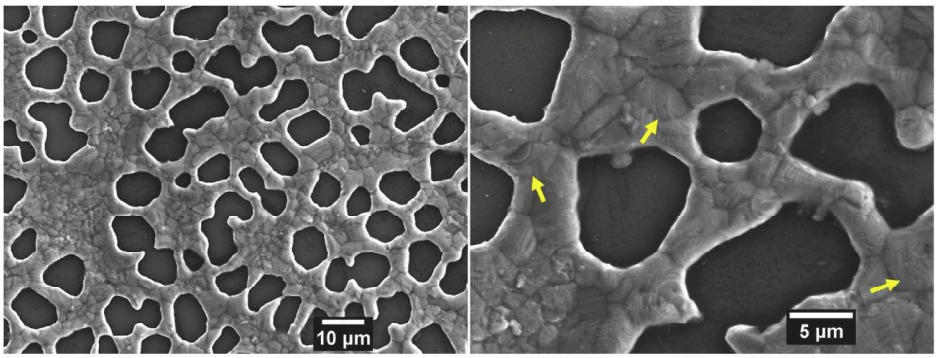

Fig. 9. Microstructure of the Cu (800 nm) / a-C (60 nm) film on SiO_2 / Si after the thermal cycle at 1000 °C and 50 sccm H_2. The arrows indicate regions with lamellar morphology.

Table 2
Average surface elemental composition (at %) of Cu films deposited under P1 and P2 conditions, obtained by energy-dispersive X-ray spectroscopy (EDS). Values correspond to the average of 4–5 measurements acquired from different surface regions.

Condition	O (%)	C (%)	Cu (%)
P1	2.2 ± 0.3	21.4 ± 41.3	96.6 ± 2.1
P2	0.55 ± 0.03	0.45 ± 0.67	97.6 ± 2.8

0.5, 1.0, 1.5, and 2.0 N. Each experimental condition was performed in triplicate to ensure reproducibility of the results. The friction tests were carried out under ambient laboratory conditions, with the temperature around 25 °C and relative humidity around 47–55 %. A schematic representing the contact mode and the reciprocating sliding parameters is shown in Fig. 2.

After the friction tests, the wear track morphologies on the surface of the Cu foils and on the counterbody (sphere) were systematically analyzed by Raman spectroscopy, 3D profilometry, and scanning electron microscopy (SEM) equipped with energy dispersive spectroscopy (EDS). The total wear volume (V, in mm^3) was determined from the cross-section profile analysis of the wear grooves obtained by 3D profilometry. From these results, the specific wear rate (k) was calculated using Eq. (1):

$$k = \frac{V(mm^3)}{P(N).s(m)} \quad (1)$$

where V represents the total wear volume in cubic millimeters (mm^3), P the applied normal load in newtons (N), and s the total sliding distance in meters (m).

3. Result and discussion

3.1. Graphene formation using a gaseous precursor

800 nm thick copper films deposited on Si substrates were used for

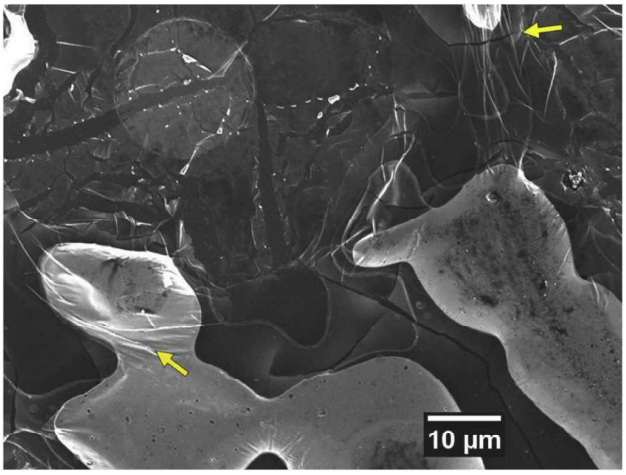

Fig. 10. SEM images of Cu/a-C films deposited under P2 conditions after annealing at 1000 °C. Remanent Cu regions are covered by multilayer graphene films; the arrows highlight wrinkles on the graphene surface.

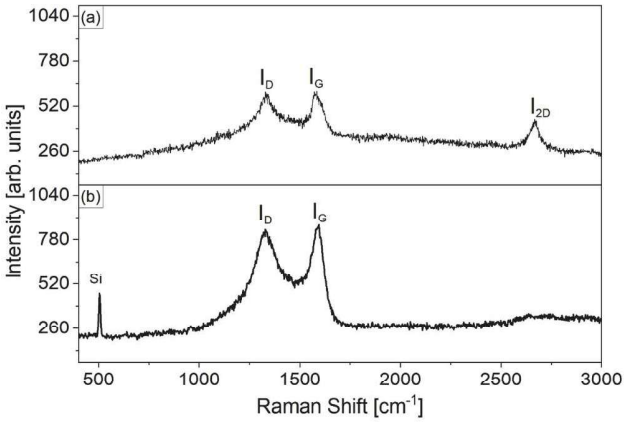

Fig. 11. Raman spectra of P2 Cu/a-C films after annealing at 1000 °C. (a) Remaining Cu regions, showing D, G, and 2D bands of multilayer graphene. (b) Substrate exposed after Cu dewetting, showing only D and G bands, with no 2D band.

graphene synthesis, under the thermal cycle conditions shown in Fig. 1 (a), with methane as the carbon precursor. The microstructure after thermal treatment revealed the formation of voids in some regions due to film removal, exposing the substrate as a consequence of temperature and processing time (Fig. 3(a)). Small regions within the grains, highlighted in the backscattered electron image, could serve as nucleation sites for carbon due to surface contamination (Fig. 3(b)). The surface morphology of the grains exhibited some wrinkles in the graphene layer (Fig. 3(c)). A closer observation of the edges of the voids allowed visualization of the graphene layer boundaries (Fig. 3(d)).

Fig. 4 presents Raman spectra from two distinct regions containing graphene. In region 1 (Fig. 4(a)), a lower defect density was observed, indicated by the lower intensity of the D band and the corresponding I_D/I_G ratio of 0.25. However, the I_{2D}/I_G ratio of 0.59 and a 2D band FWHM of 70 cm^{-1} suggest the presence of multilayer graphene. In contrast, region 2 (Fig. 4(b)) exhibited a higher defect density, with $I_D/I_G = 0.80$. The I_{2D}/I_G ratio of 1.04 and FWHM of 45 cm^{-1} indicate 2–3-layer graphene. These results demonstrate that, although the graphene layer is not entirely homogeneous, regions with low defect density and few layers suggests partial formation of structurally ordered graphene domains. Surface modifications caused by film removal during the thermal cycle, due to temperature and atmosphere, may affect graphene continuity where the catalyst is absent.

Fig. 5 shows a Raman mapping of the I_{2D}/I_G intensity ratio across a surface section of the films, highlighting the influence of microstructure on graphene layer uniformity. The optical microscopy image reveals a central region where the substrate was exposed due to film removal after thermal treatment. This variation in surface texture influenced the number of graphene layers (Fig. 5(a)). Higher I_{2D}/I_G values (>1) were observed in the central region, corresponding to bi- and tri-layer graphene. Other areas where the film remained (left side and lower right corner of the map) correspond to few-layer graphene ($0.6 < I_{2D}/I_G < 1$). Regions shown in blue in the map indicate a higher number of layers, such as multilayer graphene or graphite ($I_{2D}/I_G < 0.6$). Increased apparent roughness in regions with more layers, compared to the smoother Si substrate, demonstrates the impact of microstructure on graphene layer heterogeneity. The spectra used to construct the maps are shown in Fig. 5(b), highlighting variations in 2D band intensity across different regions.

3.2. Graphene formation using amorphous carbon

Graphene is catalyzed via a metallic film to crystallize graphene layers from an amorphous carbon film. Depending on annealing and cooling conditions, the number of graphene layers is controlled by the initial thickness of the amorphous carbon layer [3]. This formation process differs from that observed with gaseous precursors. Narula et al. [17] detailed the graphene formation using copper films as catalysts over thin amorphous carbon layers. Hydrogen plays a crucial role in graphene formation, although in a manner distinct from the gaseous precursor method. During heating (820–1020 °C), hydrogen promotes the reduction of copper oxide. At the annealing temperature, thermo-mechanical stresses induce deformation in the copper film, facilitating hydrogen transport through grain boundaries to the amorphous carbon

Table 3
Raman parameters extracted from peak fitting of graphene films obtained via methane (CH_4) and amorphous carbon (a-C) precursors, and of the of the as-deposited a-C film before annealing.

Sample / Region	Peak Position (cm^{-1})			FWHM (2D) (cm^{-1})	I_D/I_G	I_{2D}/I_G	Estimated Layers
	D	G	2D				
(a-C/Cu) – Region A (Fig. 4(a))	1331	1586	2666	46.65	0.86	~0.08	Multilayer (≥5)
(a-C/Cu) – Region B (Fig. 4(b))	1335	1585	2688	296.87	2.52	0.47	Highly disordered carbon / no graphene
(CH_4/Cu) – Region 1 (Fig. 11(a))	1321	1556	2663	70.37	0.25	0.59	Multilayer (≥5)
(CH_4/Cu) – Region 2 (Fig. 11(b))	1326	1564	2668	45.19	0.80	1.04	Few-layer graphene (2–3 layers)
Amorphous carbon (before annealing) (Fig. 7)	1405	1588	–	–	1.91	–	no graphene

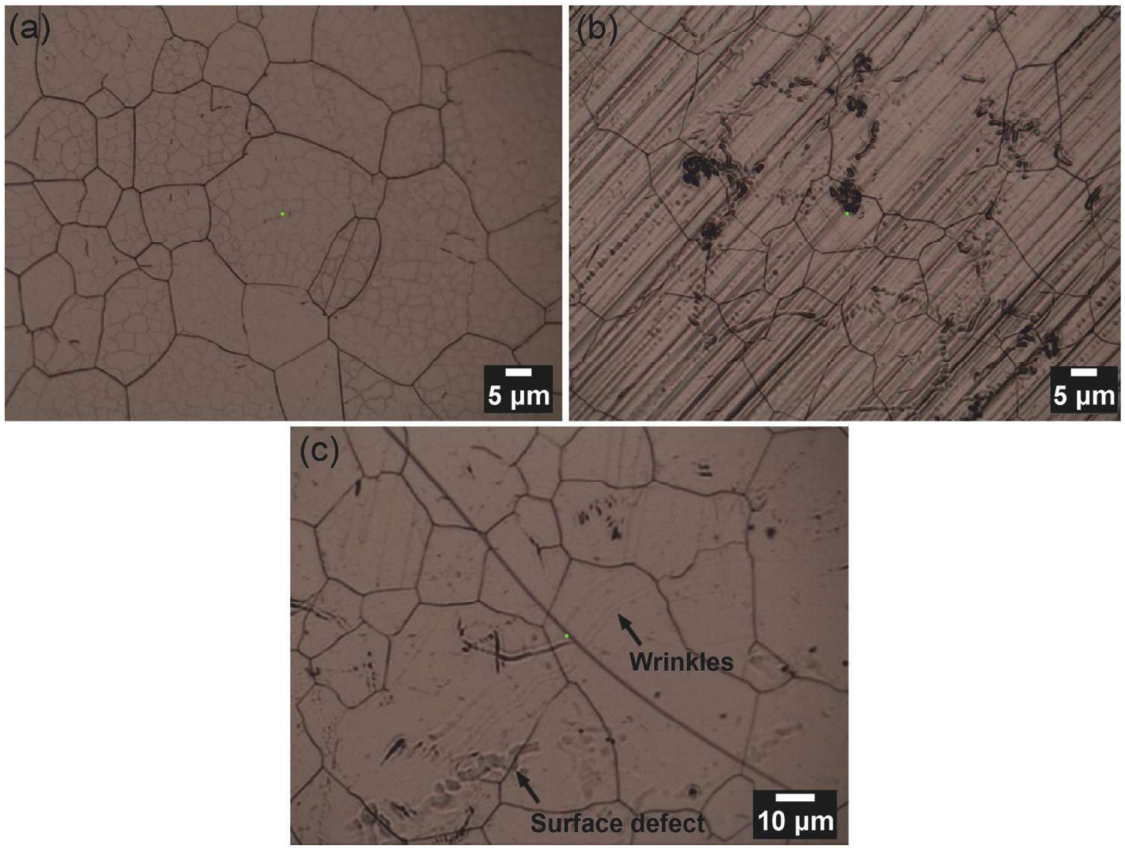

Fig. 12. Optical microscopy images of copper sheets after the thermal cycle at 1000 °C: (a) grain boundaries revealed by the thermal treatment on the polished face, (b) unpolished surface showing surface defects, and (c) detailed view of the defects and wrinkles in the graphene.

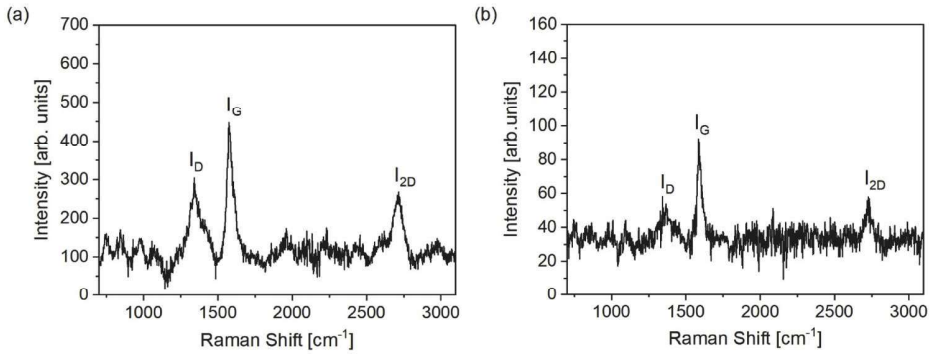

Fig. 13. Raman spectra of the surface of copper sheets after treatment: (a) center of the polished face and (b) center of the unpolished face. The background generated by Cu was subtracted for the intensity ratio calculation.

layer, forming C*/CH* radicals. These radicals diffuse along grain boundaries, promoting graphene crystallization via surface catalysis on copper.

Cross-sectional images of the copper and amorphous carbon films are shown in Fig. 6. The copper films exhibit a columnar structure, with grain growth perpendicular to the substrate surface (Fig. 6(a), secondary electron SEM). Two deposition configurations were used: (1) amorphous carbon (~58 nm) at the interface between copper (~797 nm) and the substrate (Fig. 6(b)), and (2) amorphous carbon (~58 nm) on top of copper (~745 nm) (Fig. 6(c)), backscattered electron SEM). The surface morphology of the polycrystalline copper film shows columnar grain boundaries and nodular defects, potentially formed on asperities, debris, or other external particles. These particles may originate from the reactor or substrate contamination before deposition (metallic dust, residues, or polishing debris). Surface imperfections act as preferred nucleation sites where film growth occurs faster than on the substrate [18]. In CVD with gaseous precursors, graphene nucleation with multiple layers occurs preferentially at grain boundaries due to the higher density of atomic-scale steps and curvature at the grain edges, allowing multilayer nucleation [19]. In contrast, when using a solid carbon precursor, grain boundaries serve as pathways for hydrogen transport to the amorphous carbon, generating carbon radicals necessary for graphene crystallization.

The Raman spectrum of the a-C film (Fig. 7) shows a broad band corresponding to the partial overlap of the D and G bands. Gaussian fitting revealed peaks at 1405 and 1508 cm^{-1}, respectively. The absence

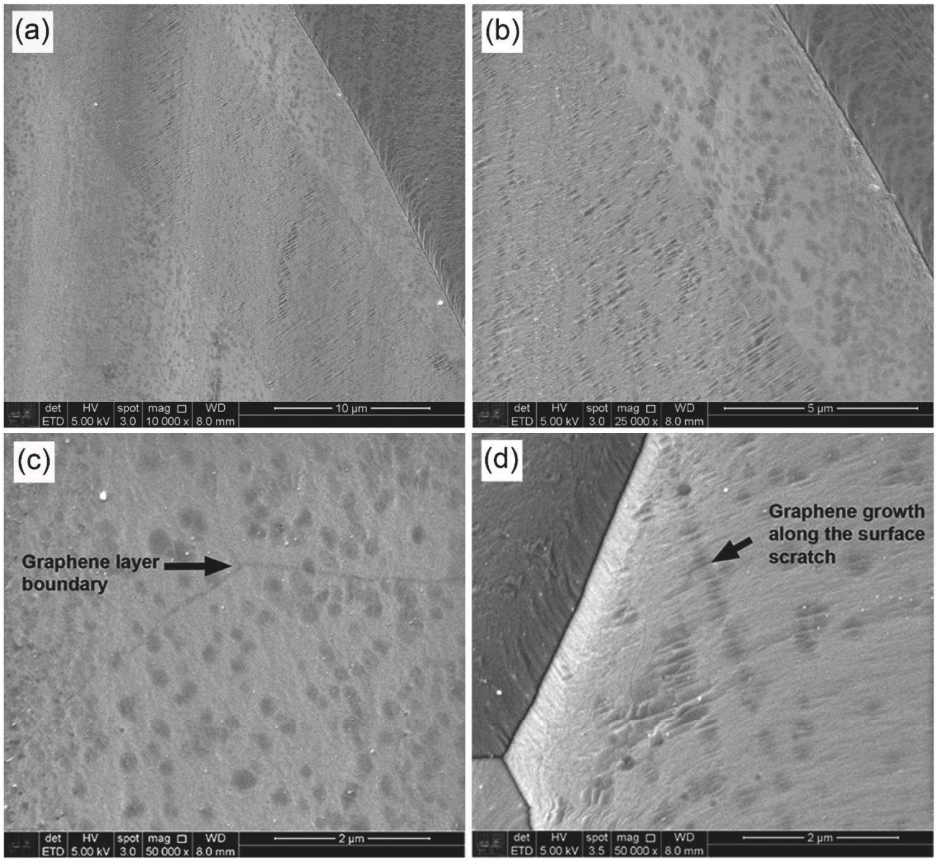

Fig. 14. SEM images of graphene island growth on copper sheets using CH_4 as carbon precursor after annealing at 1000 °C for 3 min: (a) graphene domains aligned with the mechanical texture of the copper foil, (b) preferential nucleation along copper grain and twin boundaries, (c) boundaries between adjacent graphene islands, and (d) graphene growth along a scratch on the polished surface.

of the 2D band (~2700 cm^{-1}) suggests that the films do not contain a significant amount of ordered graphene structures, neither monolayer nor multilayer [20]. The G band is associated with vibrational modes of hexagonal carbon rings, representing the main peak in graphite Raman spectra, whereas the D band reflects disorder in the graphitic structure. Analysis of these bands' positions and relative intensities allows characterization of the amorphous carbon (a-C) structure as closer to graphite-like or diamond-like than to graphene. In this case, the Raman spectrum indicates highly disordered amorphous carbon, predominantly sp^2 bonds, distorted carbon rings, and up to ~20 % sp^3 bonds. Sputtered films typically exhibit this structural configuration [21].

3.2.1. *Effect of surface morphology after the thermal cycle*

Film removal, or dewetting, is a thermally activated process in which holes form to minimize the free energy of the film, substrate, and film–substrate interface. The presence of holes, film edges, or the formation of new holes is necessary for the removal process to proceed. In the initial stage, isolated holes are generated at temperatures where the mobility of the constituent atoms is sufficiently high. These holes coalesce to either form dispersed islands or completely remove the film [22]. Bleu et al. [23] observed that during annealing of catalyst films such as nickel, the removal process is accelerated for thinner films, and the onset temperature for film removal decreases as the film thickness decreases.

Fig. 8 shows the morphologies of films with different thicknesses after annealing. Image analysis using ImageJ was performed to calculate the remaining film area fraction. Films with a thickness of 400 nm exhibited a nearly continuous network of fibrous particles after treatment at 950 °C, with a film area fraction of 24.62 % (Fig. 8(a)), and isolated rounded particles at 1000 °C, with a lower area fraction of 17.07 % (Fig. 8(b)). The thicker 1000 nm film displayed a network-like morphology after treatment at 1000 °C, but with a higher film area fraction of 28.68 % (Fig. 8(c)). Notably, at the same treatment temperature of 1000 °C, the removal process was more pronounced in the thinner film.

The microstructure of Cu/a-C films with a thickness of 800 nm deposited on SiO_2 showed considerably less film removal at 1000 °C (significantly higher remaining film area fraction of 62.66 %) (Fig. 9) compared to films deposited on silicon. A possible explanation is the modification of the silicon surface roughness due to the growth of a rougher oxide layer. Additionally, the presence of a lamellar morphology on the copper grain surface may indicate the growth of multilayer carbon.

3.2.2. *Effect of deposition conditions on film behavior after annealing*

The effect of catalyst oxidation on graphene film formation was evaluated for Cu/a-C films deposited on Si substrates under P1 (higher working pressure, lower Cu target power) and P2 (lower working pressure, higher Cu target power) conditions Table 1. The higher surface oxygen content observed for Cu films deposited under P1 can be explained by the influence of deposition parameters on Cu oxidation during sputtering (Table 2). Su et al. [24] showed that Cu can be oxidized during sputtering even under commonly used high-vacuum conditions. In their study, deposition was performed after evacuating the chamber to approximately 5×10^{-4} Pa and using 0.1 Pa of high-purity argon, yet residual oxygen and oxygen released from chamber surfaces were sufficient to oxidize sputtered Cu atoms. It was shown that lower sputtering power and higher working pressure reduce

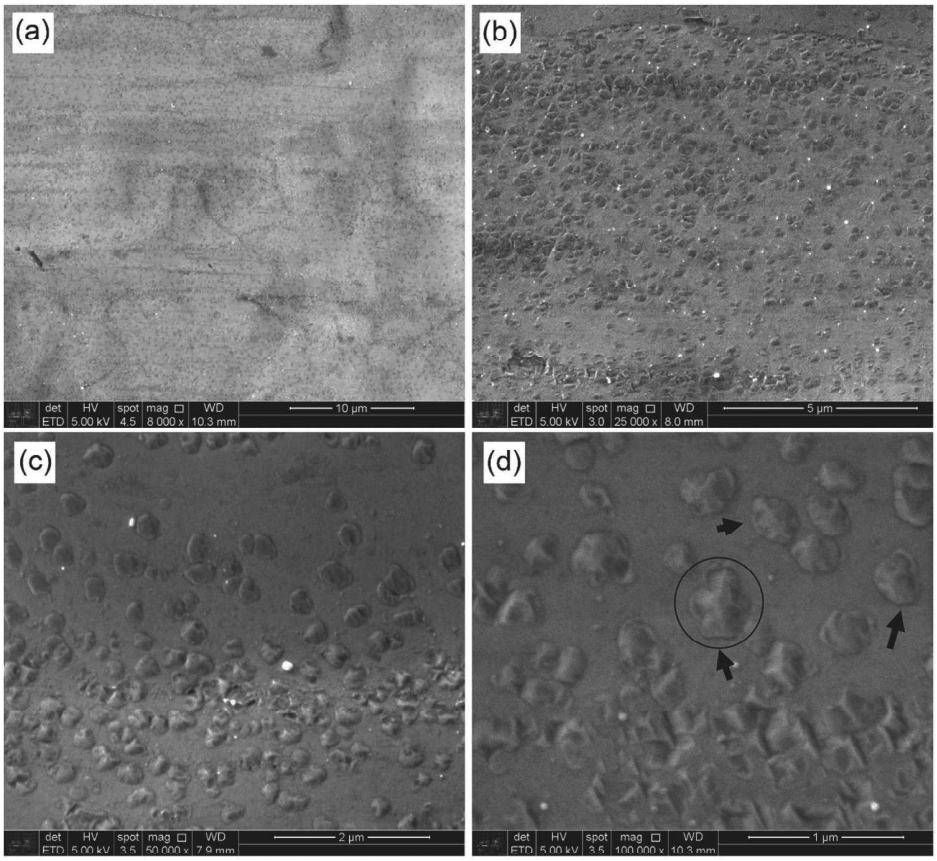

Fig. 15. SEM images of graphene islands formed on the unpolished face of copper sheets using CH_4 at 1000 °C for 15 min: (a) lower-magnification overview, (b) intragranular distribution, and (c,d) higher-magnification views of island morphology. Arrows indicate lobed islands.

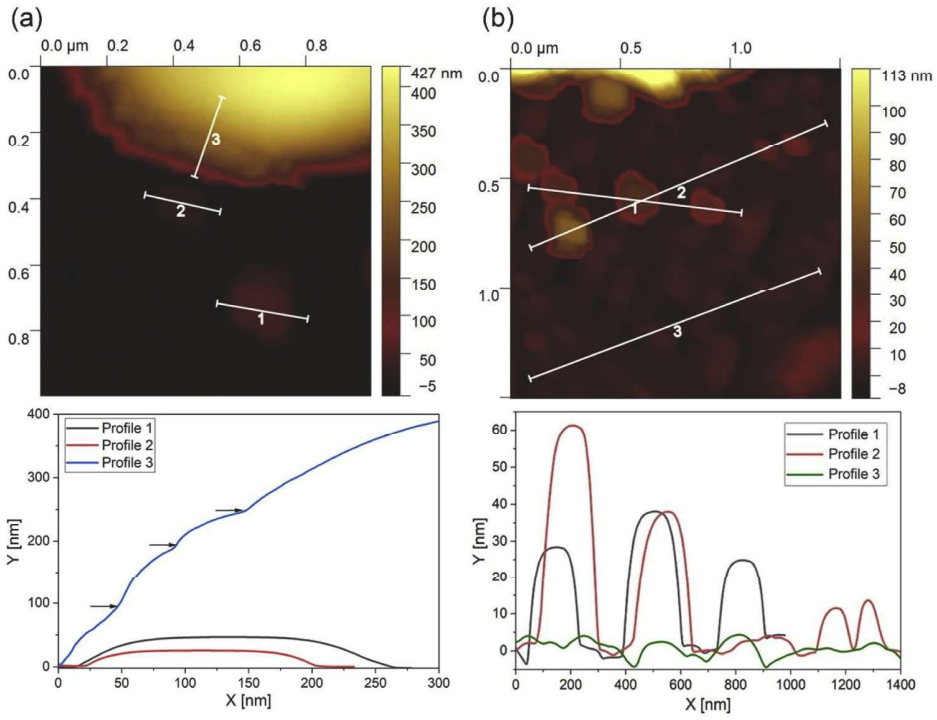

Fig. 16. AFM topography and corresponding 2D height profiles of graphene islands on Cu sheets (a) Region showing a large graphene island (>400 nm) with overlapping terraces, indicating stacked domains, (b) Region covered by thinner graphene islands (<5 nm) forming a nearly continuous film over the Cu surface.

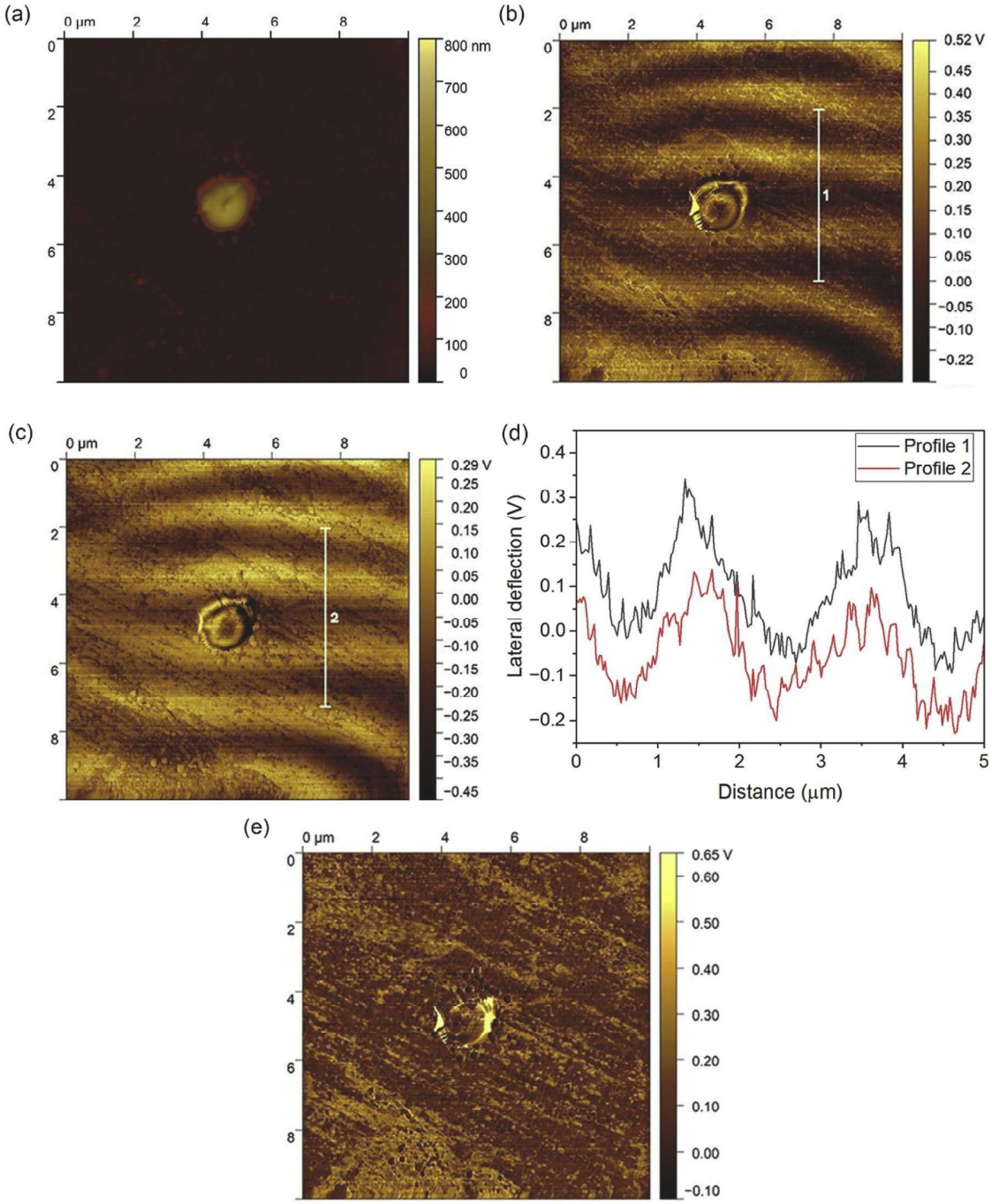

Fig. 17. AFM of graphene on copper sheets: (a) topographic image, (b) lateral deflection scan from left to right, (c) lateral deflection scan from right to left, (d) deflection profiles indicated on the lateral deflection maps, (e) friction map obtained by subtracting (c) from (b).

the effective deposition rate, thereby increasing oxidation, whereas higher power and lower pressure promote the formation of films with reduced oxygen incorporation. This behavior is consistent with our results: P1 films exhibited greater oxygen incorporation, while P2 films showed significantly reduced oxidation.

After annealing at 1000 °C, P1 films exhibited extensive dewetting, and no graphene formation was detected, which is attributed to the insufficient amount of metallic Cu remaining to catalyze graphitization. For P2 films, oxidation prior to annealing was greatly reduced, and although dewetting also occurred, remaining Cu regions persisted on the surface after thermal treatment. SEM images (Fig. 10) show that these regions are covered by graphene films that display characteristic surface wrinkles, particularly near the boundaries of the remaining Cu areas. Graphene was also observed on exposed Si between the residual Cu regions, likely formed through carbon diffusion across the Cu layer during the early stages of thermal treatment, before film retraction occurred.

Raman spectroscopy (Fig. 11) supports these observations. Spectra acquired over the remaining Cu regions display the D, G and 2D bands characteristic of multilayer graphene, whereas spectra obtained from the substrate exposed after Cu dewetting show only the D and G bands, indicating the presence of disordered carbon and the absence of

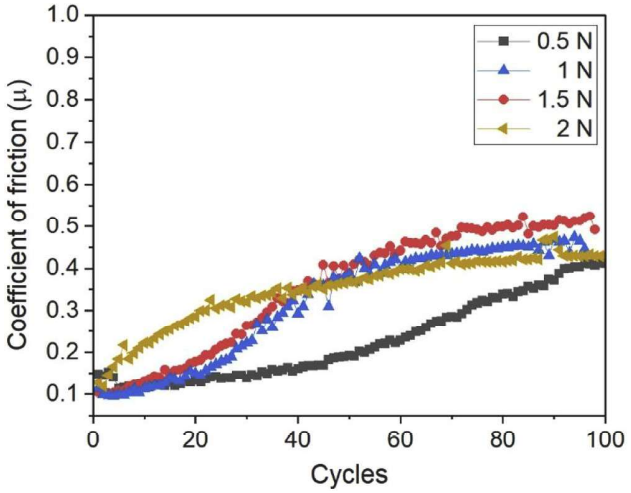

Fig. 18. Coefficient of friction curves from reciprocating sliding tests of the copper substrate with graphene against a 6 mm diameter 310 stainless steel ball, under different normal loads.

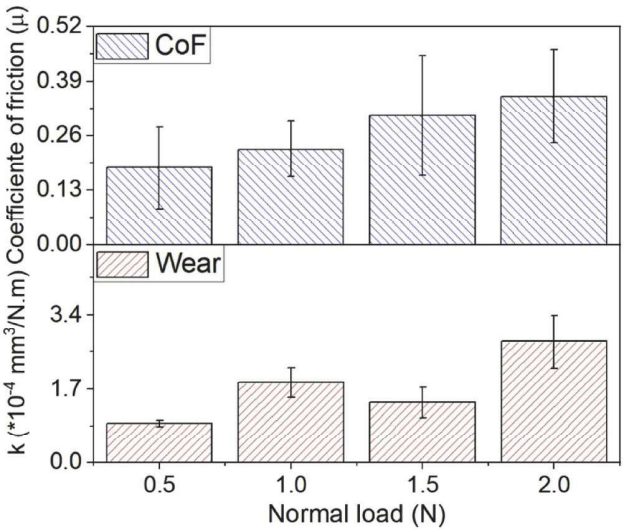

Fig. 19. Comparison of the friction coefficient (μ) and specific wear rate (k) values obtained from reciprocating sliding tests under different normal loads.

Table 4
Tribological parameters obtained from ball-on-disc tests of copper substrate with graphene under different normal loads. Average coefficient of friction (CoF); specific wear rate (k); maximum wear depth (d); wear track width (w).

Normal Load (N)	Contact Pressure (GPa)	CoF (μ)	k (*10⁻⁴ mm³/N·m)	d (μm)	w (μm)
0.5	0.40	0.18 ± 0.10	0.91 ± 0.08	0.45 ± 0.09	152.50 ± 23.85
1.0	0.50	0.23 ± 0.07	1.85 ± 0.33	1.09 ± 0.24	189.21 ± 17.62
1.5	0.58	0.31 ± 0.14	1.40 ± 0.35	1.21 ± 0.11	180.34 ± 4.88
2.0	0.63	0.35 ± 0.11	2.78 ± 0.61	1.41 ± 0.17	199.41 ± 16.71

graphene.

To provide a clear comparison of graphene films obtained from different carbon precursors, Table 3 summarizes the Raman parameters extracted from peak fitting for films synthesized via methane (CH_4) and amorphous carbon (a-C) precursors, as well as for the original amorphous carbon film prior to annealing. The table lists peak positions of the D, G, and 2D bands, 2D-band FWHM, intensity ratios I(D)/I(G) and I(2D)/I(G), and the estimated number of graphene layers. Together, these parameters enable a direct comparison of structural order across the different samples. For CH_4/Cu films, Region 1 corresponds to multilayer graphene with lower defect density, and Region 2 corresponds to 2–3-layer graphene with higher defect density, as illustrated in Fig. 4. For a-C/Cu films, Regions A and B are described in Fig. 11.

After annealing at 1000 °C, Raman spectra were fitted using line shapes appropriate for the expected degree of structural order in each material. The amorphous carbon (a-C) film prior to annealing was fitted with Gaussian functions, reproducing the broad and heavily overlapped D and G bands characteristic of highly disordered carbon. In contrast, graphene-like regions after annealing were fitted with Lorentzian functions, which better represent the narrower and more symmetric vibrational modes of sp^2-bonded carbon in crystalline or few-layer graphene [10]. The I(D)/I(G) ratios reported correspond to peak height ratios derived from these fits.

The samples derived from the amorphous-carbon route exhibit a broad range of structural order: the pristine a-C film shows a high I(D)/I(G) ratio (1.91), consistent with its strongly disordered nature. After annealing, a-C/Cu films display both moderately disordered multilayer graphene (Region A, I(D)/I(G) = 0.86) and regions of severe disorder where no graphene is formed (Region B, I(D)/I(G) = 2.52), reflecting variations in Cu coverage during dewetting. In contrast, CH_4/Cu films show overall lower defect densities, with Region 1 exhibiting the smallest I(D)/I(G) ratio (0.25) and Region 2 showing intermediate disorder (I(D)/I(G) = 0.80), consistent with 2–3-layer graphene. These variations reflect differences in local Cu coverage, catalytic uniformity, and carbon supply during growth.

This comparative analysis shows that, under the annealing conditions employed in this study, methane-derived films consistently exhibit lower defect density and fewer layers, whereas amorphous-carbon-derived films produce multilayer graphene only in regions with sufficient Cu coverage and highly disordered carbon where catalyst continuity is disrupted. The amorphous carbon film prior to annealing serves as a reference for the initial structural disorder before graphitization. It should be noted that differences in annealing time, Cu dewetting behavior, gas flow, and chamber cleanliness may also significantly influence the resulting graphene quality.

3.3. Graphene formation on copper foils

Fig. 12 shows optical microscopy images of copper foil surfaces after thermal treatment at 1000 °C for 3 min, using a methane and hydrogen atmosphere as precursor gases. The low solubility of carbon in copper limits carbon growth and favors the formation of graphene monolayers (or, depending on conditions, bilayers or trilayers) with randomly oriented domains [7]. These domains expand over time to form polycrystalline graphene sheets. The polished surface (Fig. 12(a)) exhibits fewer defects compared to the unpolished surface (Fig. 12(b)). Surface contamination and a higher number of grain boundaries in polycrystalline materials act as preferential nucleation sites for graphene [6]. In Fig. 12(c), wrinkles in the graphene layer and macroscopic defects, such as scratches or contaminated regions, are observed. Annealing twins, typical of face-centered cubic metals, may act as boundaries for graphene nucleation. Wrinkle formation can be attributed to the mismatch in thermal expansion coefficients between copper and graphene [25].

Raman spectroscopy provides insights into the graphene microstructure. The characteristic bands include: the G band (~1580 cm^{-1}), associated with in-plane sp^2 C–C stretching modes; the D band (~1350 cm^{-1}), related to lattice defects and graphene edges; and the 2D band

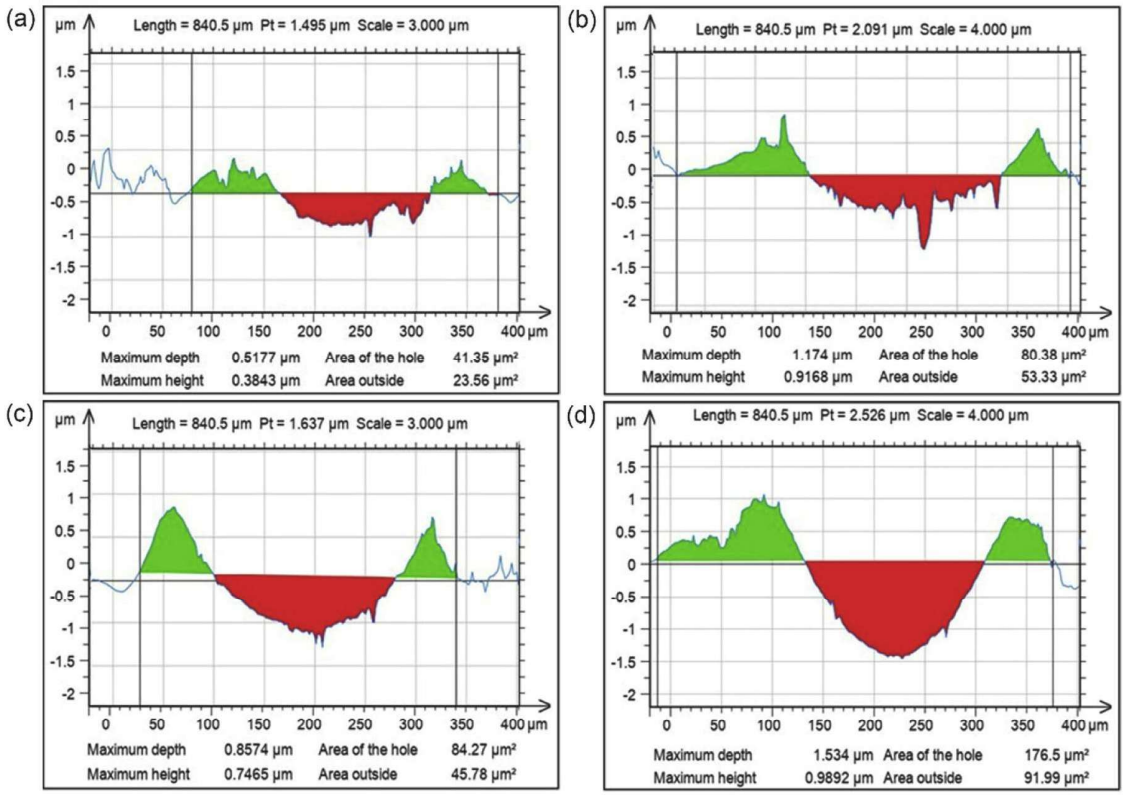

Fig. 20. 2D profiles of the wear track on the copper sheet with graphene, obtained from reciprocating sliding tests against a 6 mm diameter 310 stainless steel ball, under different normal loads: (a) 0.5 N, (b) 1 N, (c) 1.5 N, and (d) 2 N.

(~2700 cm^{-1}), a second-order two-phonon mode associated with graphene and graphite [9]. The relative intensity of the D band (I_D/I_G) indicates defect density, while the I_{2D}/I_G ratio estimates the number of layers: values >1 suggest monolayer, ~0.6 multilayer, and <1 trilayer [26,27]. The shape and width of the 2D band (FWHM) are also correlated with the number of layers, varying from 30 to 40 cm^{-1} for 1–2 layers to ~60 cm^{-1} for ~4 layers [28].

Raman spectra of copper foils after catalysis indicate the formation of multilayer graphene with moderate defects (Fig. 13). For the unpolished side, $I_{2D}/I_G = 0.68$, $I_D/I_G = 0.66$, and FWHM = 67 cm^{-1} were obtained (Fig. 13(a)). On the polished side, a spectrum of lower intensity was obtained at the center of the sample, indicating that surface roughness contributes to the greater formation of graphene (Fig. 13(b)). For the polished side, $I_{2D}/I_G \approx 0.6$, $I_D/I_G \approx 0.55$, and FWHM = 45 cm^{-1}. These results suggests that fewer defects and grain boundaries in the graphene were observed, although contamination and growth parameters influenced nucleation density and the number of layers at the center of the unpolished side.

Graphene microstructure is further detailed in high-resolution SEM images (Fig. 14). Graphene domains are observed growing along the mechanical texture of the foil (Fig. 14(a)), with preferential nucleation occurring along the copper grain boundaries and twin boundaries (Fig. 14(b)), which act as active sites for domain initiation and growth. Interlayer boundaries between graphene islands are also visible (Fig. 14 (c)). Graphene islands develop along scratches on copper grains (Fig. 14 (d)), frequently exhibiting near-hexagonal shapes inherited from the crystalline structure of graphene. However, alternative morphologies may arise depending on hydrogen partial pressure, including quadrilobed, triangular, pentagonal, or 12-lobed domains [29]. Hydrogen acts as a co-catalyst, generating active carbon species (CyHx) and controlling grain shape and size by removing weak bonds. Hexagonal grains with zigzag edges form under higher hydrogen pressures, limiting grain size, whereas lower pressures yield diverse morphologies without edge preference.

With longer treatment times (15 min), island density increases significantly (Fig. 15(a)). Intragranular distributions (Fig. 15(b)) and higher-magnification views of island contours (Fig. 15(c) and Fig. 15(d)) reveal irregular edges, suggesting a low P_{H2}/P_{CH4} ratio. Some islands exhibit lobed morphologies, indicative of surface-diffusion-limited growth. The crystallographic texture of the copper foil and local defects promote preferential nucleation and distinct rotational domains. Topographic steps and terrace bunching induce variations in graphene orientation, generating internal boundaries and asymmetric shapes, including lobed structures with sixfold symmetry. Even at high temperatures, local perturbations continue to influence island morphology [30].

Fig. 16 presents images obtained by atomic force microscopy (AFM) in intermittent mode, aimed at characterizing the surface morphology of copper sheets partially covered by graphene. In Fig. 16(a), a graphene island with dimensions larger than 400 nm is observed, noticeably larger than the other islands present in the region. The height profile along this island reveals significant variation, with successive steps or terraces indicating the presence of overlapping layers. This morphology suggests the existence of different stacked domains, possibly due to the growth and presence of defects on the copper sheet surface during deposition. In Fig. 16(b), it is observed that the base of the copper sheet is covered by thinner islands, with heights below 5 nm (graphene with fewer layers), forming a continuous film over the surface. These islands contrast with other structures in the same region, which have thicknesses between 20 and 50 nm. This pattern may be related to a low ratio between hydrogen and methane partial pressures (pH_2/P_{CH_4}) during growth, favoring the formation of reactive edges and anisotropic lateral growth.

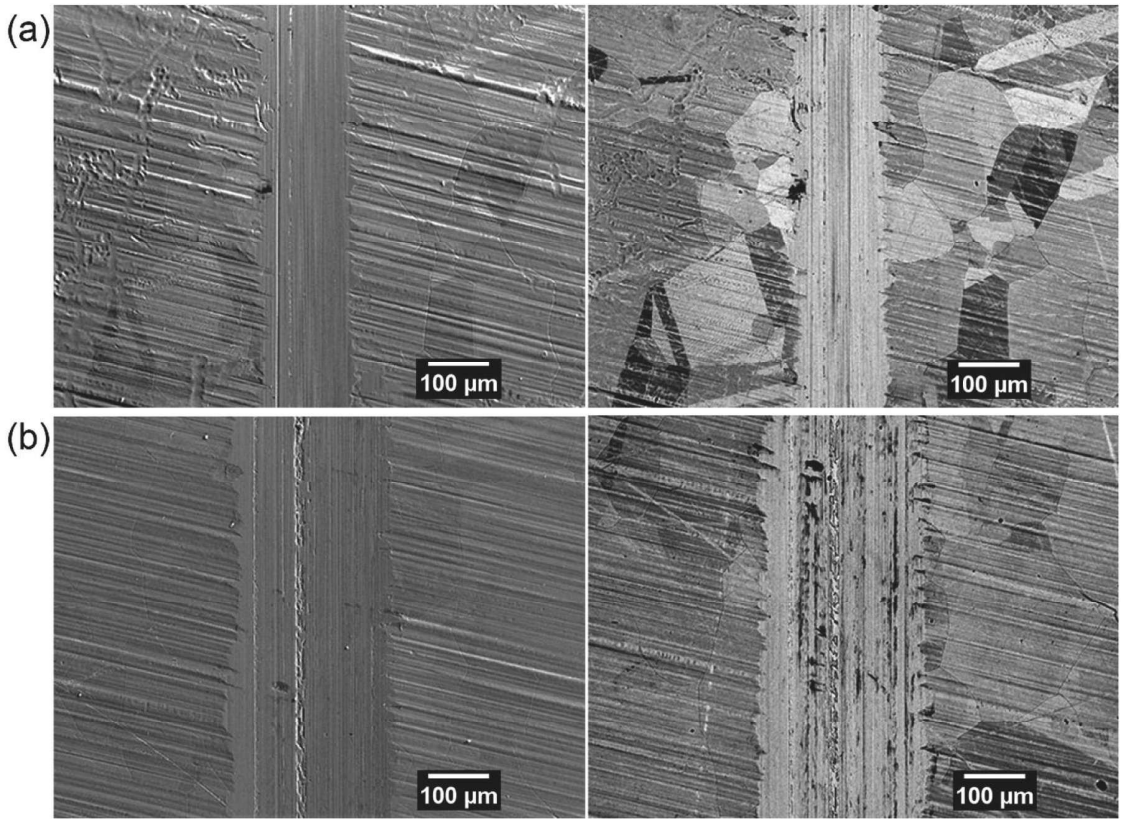

Fig. 21. SEM images in secondary electrons (left) and backscattered electrons (right) of the wear track on the copper sheet with graphene under different normal loads: (a) 0.5 N, and (b) 2 N.

3.3.1. *AFM lateral-friction mapping*

Fig. 17 presents the atomic force microscopy (AFM) analysis using lateral-friction contrast, obtained in contact mode through the lateral deflection of the cantilever. The topographic image (Fig. 17(a)) shows the analyzed region, where height profiles had previously identified a graphene island with a larger number of layers. Fig. 17(b) and Fig. 17(c) correspond to forward (trace) and backward (retrace) lateral deflection scans, respectively. Both images display a periodic pattern of bright and dark stripes across the surface, which can be attributed to the relief of the cold-rolled copper foil. This strong background signal complicates the direct interpretation of friction contrast related to graphene.

To evaluate the influence of the copper surface roughness on the friction signal, two representative line profiles (Profiles 1 and 2) were extracted along the undulated regions in both trace and retrace images (Fig. 17(d)). The deflection, expressed in volts, exhibits higher amplitudes in bright areas and lower values in dark areas, reflecting lateral variations during scanning but not yet conclusively linked to the presence of graphene.

To isolate the effect of surface topography and highlight the graphene contribution, a subtraction between the trace and retrace images was performed (Fig. 17(e)), following the procedure described in the literature [16]. The resulting contrast reveals an extended dark region associated with lower friction, which is interpreted as a dispersed graphene layer covering most of the analyzed area. This low-friction region also includes the thicker graphene island previously identified in the topographic image. In contrast, regions of smaller area and higher brightness are observed surrounding the graphene island. These regions are attributed to exposed copper, which exhibits relatively higher friction compared to the graphene-covered surface.

The roughness analysis indicates reduced RMS values on graphene-coated areas compared to bare copper, consistent with smoother contact surfaces and improved lubricating performance. The presence of multiple domains with distinct thicknesses results in a heterogeneous tribological response: continuous, few-layer graphene patches act as effective lubricating sites, while thicker or irregular islands may increase asperity interactions, contributing to local friction variations.

From the results obtained, it becomes clear that local graphene morphology exerts a significant influence on friction at the microscale. Through the combined use of AFM lateral-friction mapping and Raman characterization, heterogeneity in graphene layer thickness and surface coverage was shown to affect the spatial distribution of friction across the surface. This integrated analysis provides insight beyond previous macroscale studies, in which only average friction and wear values are typically reported without spatial resolution. The results also show that even within nominally continuous graphene films, regions with fewer layers or with structural defects contribute differently to friction, highlighting the critical role of microstructural heterogeneity in governing tribological behavior. Establishing this correlation between microstructure and frictional response represents a meaningful advancement toward understanding graphene's lubricating mechanisms under realistic contact conditions, helping to bridge the gap between nanoscale observations and macroscale performance.

3.3.2. *Macroscale tribological characterization*

Although most tribological studies involving graphene have been conducted at the micro- and nanoscale, there has been increasing interest in the past decades in assessing its performance under contact conditions more representative of real or industrial applications. Recent results confirm that graphene films can act as effective solid lubricants also at the macroscale, significantly reducing both friction and wear, even under dry conditions [31,32]. In particular, graphene has been shown to maintain low friction coefficients (~0.15) and reduce wear by

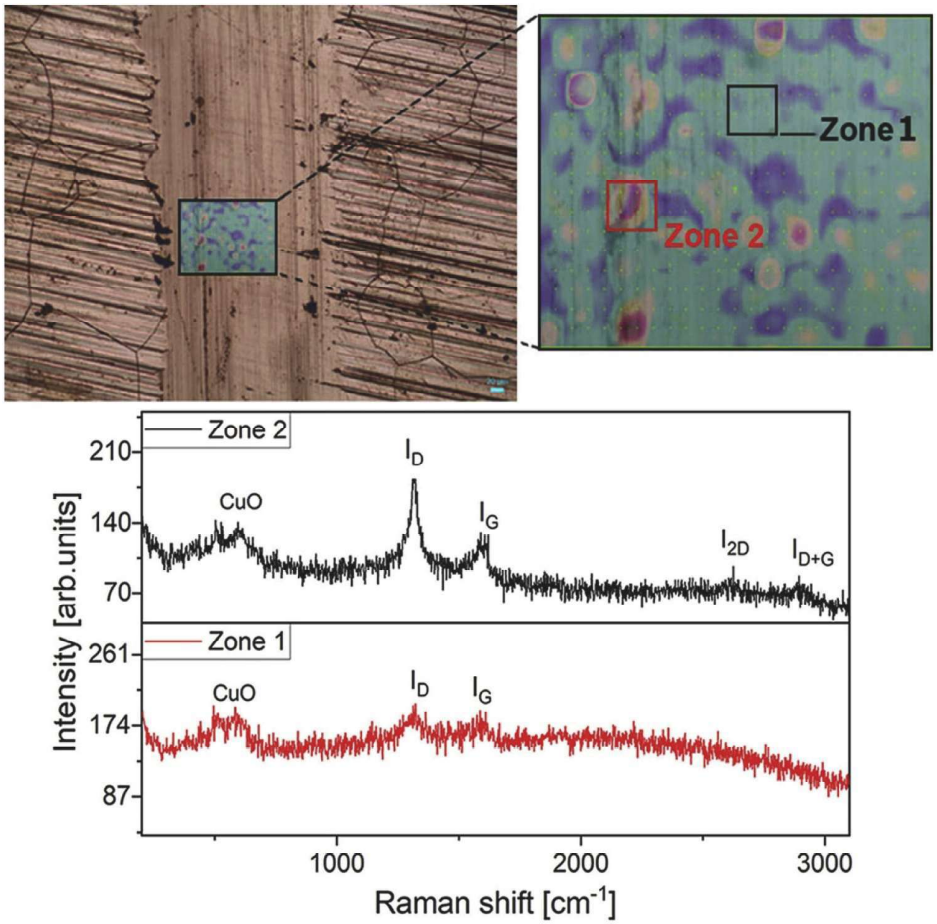

Fig. 22. Raman spectra from two regions within the wear track of the copper sheet with graphene after 100 sliding cycles under a normal load of 1.5 N. The measurements were performed using a 638 nm laser.

up to four orders of magnitude compared to bare steel, even in low-humidity environments [33]. However, the tribological performance of graphene at the macroscale strongly depends on load conditions and environment, as ultrathin layers can be progressively removed under high loads, leading to increased friction and degradation into disordered graphitic structures. Against this backdrop, the present investigation aims to evaluate the influence of graphene layers grown directly on 0.25 mm-thick copper foils, approaching bulk behavior, on friction and wear at the macroscale under different normal loads.

Fig. 18 presents the evolution of the coefficient of friction (CoF) as a function of the number of sliding cycles for different normal loads, measured on copper foil after graphene formation. Initially, the CoF remains low due to the protective graphene layer; however, with repeated sliding, the layer is progressively removed, exposing the underlying copper and leading to increased friction. The average CoF increased from 0.18 ± 0.10 at the lowest load (0.5 N, maximum Hertzian contact pressure of 0.40 GPa) to 0.35 ± 0.11 at the highest load (2.0 N, 0.63 GPa), reflecting the progressive loss of the protective graphene layer under higher contact stresses. The comparison of average CoF values for each load condition is summarized in Fig. 19 and Table 4, highlighting the effect of increasing normal load on friction.

Wear track profiles obtained by optical profilometry (Fig. 20) show a progressive increase in track depth and width with increasing normal load, reflecting more pronounced material removal and graphene degradation. Maximum wear depth and specific wear rate also increased with load, from 0.45 ± 0.09 μm and 0.91 ± 0.08 × 10^{-4} mm^3/N·m at 0.5 N to 1.41 ± 0.17 μm and 2.78 ± 0.61 × 10^{-4} mm^3/N·m at 2.0 N. Wear track width similarly increased with load. Even under the lowest load, the wear depth exceeds the typical thickness of few-layer graphene (<10 nm), indicating penetration to the copper substrate. At higher loads, after the graphene layer is removed, wear occurs mainly on the exposed copper substrate, which now governs the friction and material removal. The data in Table 4 reflect these trends along with the measured standard deviations for each parameter.

Fig. 21 presents SEM images using both secondary and backscattered electrons, showing significant differences between wear tracks formed under 0.5 N and 2 N after 100 sliding cycles. In particular, the track width increases considerably at the highest load. Under 2 N, the surface shows pronounced dark grooves within the track, likely caused by localized oxidation and debris accumulation, which are not evident under 0.5 N.

Raman spectroscopy tests after 100 cycles at an intermediate load of 1.5 N further support these observations, as indicated in (Fig. 22). Spectral analysis of abrasive zones (zone 1 and zone 2) indicates the absence of the 2D band (~2700 cm^{-1}), traditionally associated with crystalline graphene, indicating structural modification and distortion. A pronounced increase in the D peak (~1350 cm^{-1}), representing defects and network disorder, suggests a trend toward amorphization due to mechanical wear [33,34]. Additionally, the presence of the D + G combined peak in zone 2, possibly due to graphene oxidation, reinforces the hypothesis of progressive chemical degradation of the protective layer during prolonged sliding. This structural and chemical modification is widely documented as a mechanism compromising lubricant layer stability, favoring gradual exposure of the metallic substrate [13].

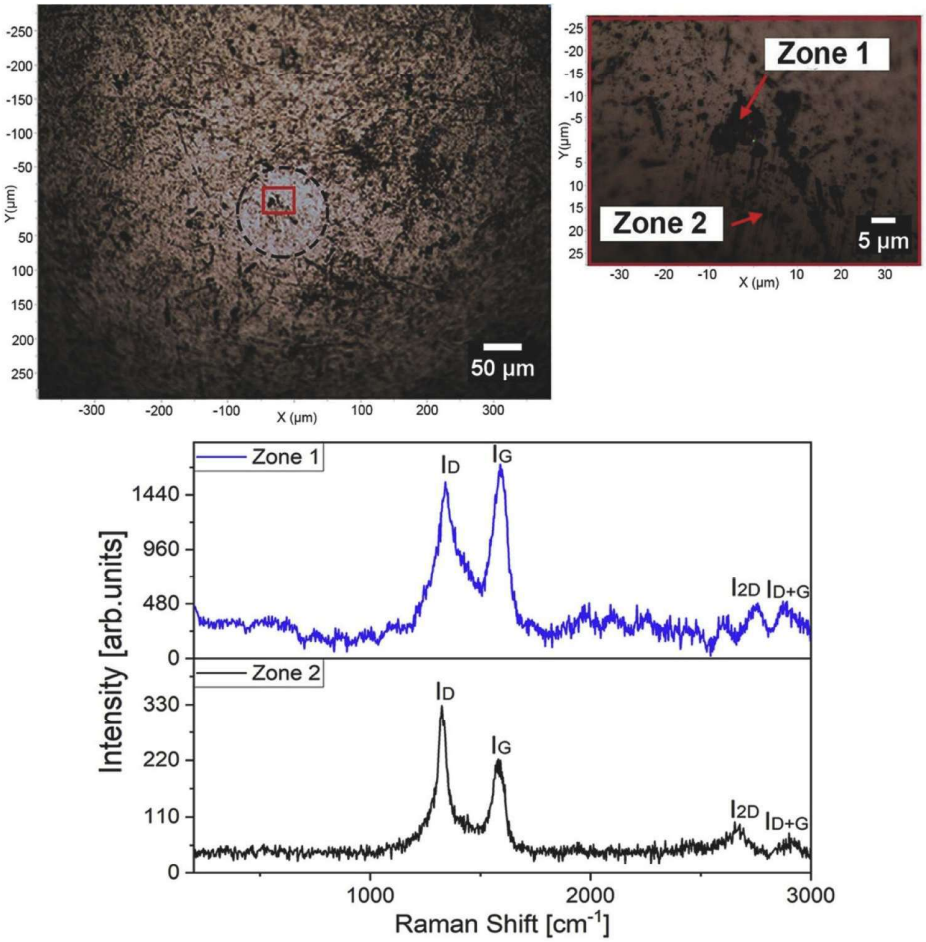

Fig. 23. Raman spectra from two regions on the wear scar surface of the 310 stainless steel ball after 100 sliding cycles under a normal load of 1 N. The measurements were performed using a 638 nm laser.

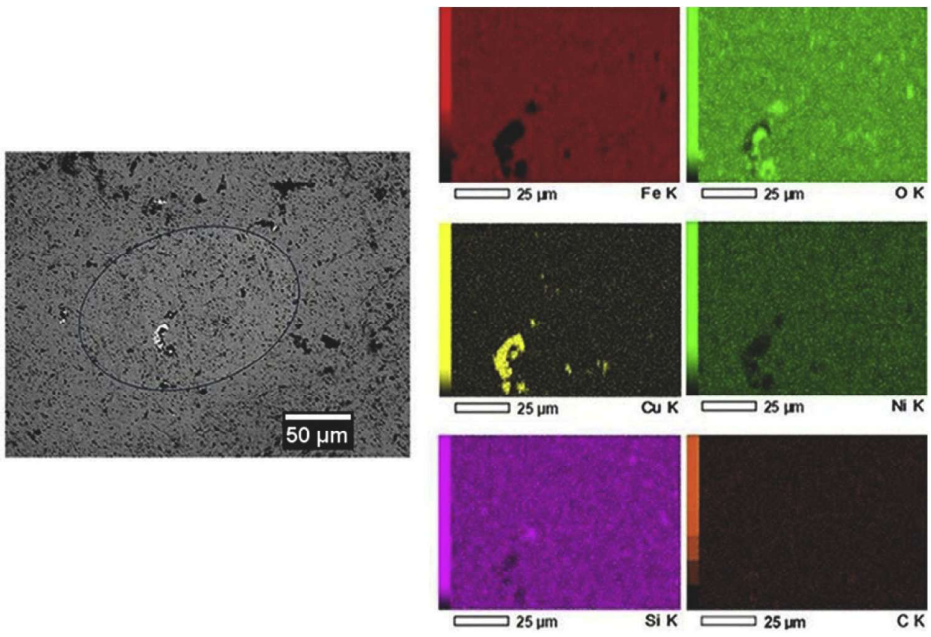

Fig. 24. EDS map of the wear surface of the 310 stainless steel ball after 100 sliding cycles under a normal load of 1.5 N.

Copper oxide (CuO) was also detected, with a characteristic peak near 600 cm^{-1}, indicating that wear promotes oxidation of the underlying copper surface under higher loads. These observations are consistent with dark grooves observed in SEM and debris formation, showing that the initial graphene protection is insufficient under high-load and prolonged sliding conditions.

Graphene degradation under sliding is a complex process involving progressive structural disorder. As described by Ferrari & Robertson [21], this evolution typically follows a transition from crystalline graphite to amorphous carbon via a nanocrystalline graphite phase. This transformation is marked by changes in the Raman G and D bands, such as peak shifts and intensity variations, reflecting increased defect density, altered chemical bonding, and reduced domain size. These structural modifications directly affect vibrational and electronic properties, resulting in tribological changes like increased friction and surface wear. The formation of a defect-rich, amorphous carbon layer compromises the integrity of the graphene, limiting its effectiveness as a solid lubricant and protective barrier.

In addition to structural degradation, chemical alterations can occur during sliding, especially in the presence of oxygen or humidity. These tribochemical reactions modify surface composition, leading to oxidation of both the graphene and the underlying metal. The resulting formation of oxides and oxygenated functional groups increases surface roughness and weakens layer adhesion, ultimately raising friction and wear. Together, amorphization and chemical oxidation accelerate graphene degradation, reducing its durability in macroscale tribological applications [14].

Raman spectra collected from two distinct zones within the wear scar on the 310 stainless steel ball, used as the counterbody against graphene-copper foil (Fig. 23), reveal further insight into this degradation. In Zone 1, within localized transferred debris, the D band shows moderate intensity ($I_D/I_G = 0.9$), indicating structural disorder. In Zone 2, associated with a separate debris area, the D band is even more intense ($I_D/I_G > 1$), suggesting higher disorder or oxidation. Notably, both regions exhibit the D + G combination band following the 2D band, pointing to chemical modifications, particularly oxidation, accompanying structural damage.

The Raman spectra collected with a 638 nm laser show an unusually high D/G intensity ratio ($I_D/I_G > 1$), especially in the worn regions. This behavior is attributed to two combined effects: (i) the presence of structural defects and partial amorphization of the graphene fragments transferred to the steel surface, and (ii) the wavelength-dependent nature of the D band, which is enhanced at longer excitation wavelengths due to the increased efficiency of the defect-activated double-resonance Raman process [35]. These results suggest that both mechanical wear and possible oxidation significantly disrupted the sp^2 lattice, increasing the defect density.

Surface analysis of the 310 stainless steel spheres after the sliding test at 1.5 N and 50 cycles via EDS elemental mapping revealed transfer of copper particles from the softer substrate to the sphere, indicating partial adhesion of the softer material during sliding. A higher oxygen concentration region was also detected on the sphere surface, suggesting localized oxidation. Despite these phenomena, only a minor amount of wear debris adhered to the sphere after 100 cycles, suggesting relatively moderate wear or efficient removal of detached particles during testing (Fig. 24).

Tribological evaluation through Raman spectroscopy and SEM analyzes of the wear tracks indicate that while graphene initially acts as an effective barrier against wear and reduces friction, its performance deteriorates with increasing load and contact time, which was also observed in other studies on multilayer graphene films on metallic surfaces [15]. The result is the formation of a transfer layer composed of distorted graphene fragments tending towards amorphous carbon, along with substrate oxidation, contributing to increased friction under extended sliding. Recent studies show that doping with Ti, Al, or Si can modulate the balance between friction-induced graphitization and tribochemical oxidation, promoting formation of transfer films with lower friction and greater durability [36,37]. While the present work focused on direct application of graphene on copper, these technological alternatives suggest paths for developing hybrid or modified coatings capable of overcoming current limitations in graphene stability under macroscale tribological conditions.

4. Conclusions

Graphene layers were successfully synthesized on copper foils and sheets using both CVD and PVD approaches, with the choice of carbon precursor and processing conditions strongly influencing layer morphology, number of layers, and coverage. On copper sheets, CVD growth led to the formation of thicker graphene islands along the surface texture, with surface roughness and local defects contributing to multilayer nucleation. Annealed copper films produced few-layer graphene with heterogeneous coverage. In contrast, amorphous carbon/copper films showed that longer thermal treatments enhanced film removal, and graphene formation depended on hydrogen-mediated reactions at the interface. SEM imaging revealed surface voids and morphological features caused by film retraction, confirming heterogeneous coverage. Raman mapping provided further evidence of local variations in layer number and defect density, highlighting areas of multilayer graphene and structural irregularities.

AFM analysis on copper sheets revealed irregular graphene islands with significant thickness variations. Friction maps indicated notable local reductions in friction in regions covered by graphene, and subtraction of lateral force maps confirmed that these differences were primarily due to the graphene rather than the underlying surface roughness.

Macroscale sliding tests demonstrated that graphene effectively reduces the friction coefficient under low normal loads, but its protective function diminishes at higher loads due to mechanical wear. Raman and spectroscopic analyses confirmed progressive structural and chemical degradation of the graphene layer, including amorphization and oxidation, which compromise its tribological performance.

These results provide a comprehensive understanding of graphene growth on copper substrates, its surface morphology, and its friction and wear behavior, offering insights for macroscale applications where thin graphene layers may act as solid lubricants or protective coatings.

CRediT authorship contribution statement

M.F.C. Ordoñez: Writing – original draft, Visualization, Validation, Supervision, Project administration, Methodology, Investigation, Funding acquisition, Formal analysis, Data curation, Conceptualization. **D.J. Feria:** Writing – original draft, Validation, Methodology, Investigation, Formal analysis. **I. Pereyra:** Writing – original draft, Resources, Methodology, Investigation, Formal analysis. **M.N.P. Carreño:** Writing – original draft, Validation, Resources, Methodology, Investigation, Formal analysis. **R.M. Souza:** Writing – original draft, Supervision, Resources, Formal analysis, Conceptualization. **A.P. Tschiptschin:** Writing – original draft, Supervision, Resources, Project administration, Methodology, Investigation, Funding acquisition, Formal analysis, Conceptualization.

Declaration of competing interest

The authors declare that they have no known competing financial interests or personal relationships that could have appeared to influence the work reported in this paper.

Acknowledgements

This study was financed, in part, by the São Paulo Research Foundation (FAPESP), Brasil. process number 2023/07548–3.

Data availability

Data will be made available on request.

References

[1] A.K. Geim, K.S. Novoselov, The rise of graphene, Nat. Mater. 6 (2007) 183–191, https://doi.org/10.1038/nmat1849.

[2] A.K. Geim, Graphene: status and prospects, Science 324 (2009) 1530–1534, https://doi.org/10.1126/science.1158877.

[3] M. Zheng, K. Takei, B. Hsia, H. Fang, X. Zhang, N. Ferralis, H. Ko, Y.L. Chueh, Y. Zhang, R. Maboudian, A. Javey, Metal-catalyzed crystallization of amorphous carbon to graphene, Appl. Phys. Lett. 96 (6) (2010) 063110, https://doi.org/10.1063/1.3318263.

[4] J. Hofrichter, B.N. Szafranek, M. Otto, T. Echtermeyer, M. Baus, A. Majerus, V. Geringer, M. Ramsteiner, H. Kurz, Synthesis of graphene on silicon dioxide by a solid carbon source, Nano Lett. 10 (1) (2010) 36–42, https://doi.org/10.1021/nl902558x.

[5] W. Liu, H. Li, C. Xu, Y. Khatami, K. Banerjee, Synthesis of high-quality monolayer and bilayer graphene on copper using chemical vapor deposition, Carbon N Y 49 (2011) 4122–4130, https://doi.org/10.1016/j.carbon.2011.05.047.

[6] G.H. Han, F. Güneş, J.J. Bae, E.S. Kim, S.J. Chae, H. J.Shin, J.Y. Choi, D. Pribat, Y. H. Lee, Influence of copper morphology in forming nucleation seeds for graphene growth, Nano Lett. 11 (10) (2011) 4144–4148, https://doi.org/10.1021/nl201980p.

[7] I. Vlassiouk, M. Regmi, P. Fulvio, Role of hydrogen in chemical vapor deposition growth of large single-crystal graphene, ACS Nano 5 (7) (2011) 6069–6076, https://doi.org/10.1021/nn201978y.

[8] R. Vishwakarma, S. Mondal, G. Kalita, H. Uchida, M. Tanemura, *Transfer free graphene growth on SiO_2 substrate at 250 °C*, Appl. Surf. Sci. 403 (2017) 420–425, https://doi.org/10.1038/srep43756.

[9] A.C. Ferrari, J.C. Meyer, V. Scardaci, C. Casiraghi, M. Lazzeri, F. Mauri, S. Piscanec, D. Jiang, K.S. Novoselov, S. Roth, A.K. Geim, Raman spectrum of graphene and graphene layers, Phys. Rev. Lett. 97 (18) (2006) 187401, https://doi.org/10.1103/PhysRevLett.97.187401.

[10] J.B. Wu, M.L. Lin, X. Cong, H.N. Liu, P.H. Tan, Raman spectroscopy of graphene-based materials and its applications in related devices, Chem. Soc. Rev. 47 (5) (2018) 1822–1873, https://doi.org/10.1039/C6CS00915H.

[11] D. Marchetto, C. Held, F. Hausen, F. Wählisch, M. Dienwiebel, R. Bennewitz, Friction and wear on single-layer epitaxial graphene in multi-asperity contacts, Tribol. Lett. 48 (1) (2012) 77–82, https://doi.org/10.1007/s11249-012-9945-4.

[12] K.S. Kim, H.J. Lee, C. Lee, S.K. Lee, J.H. Jang, J.H. Ahn, J.H. Kim, H.J. Lee, Chemical vapor deposition-grown graphene: the thinnest solid lubricant, ACS Nano 5 (6) (2011) 5107–5114, https://doi.org/10.1021/nn2011865.

[13] D. Berman, A. Erdemir, A.V. Sumant, Few layer graphene to reduce wear and friction on sliding steel surfaces, Carbon N Y 54 (2013) 454–459, https://doi.org/10.1016/j.carbon.2012.11.061.

[14] M.S. Won, O.V. Penkov, D.E. Kim, Durability and degradation mechanism of graphene coatings deposited on Cu substrates under dry contact sliding, Carbon N Y 103 (2013) 57–64, https://doi.org/10.1016/j.carbon.2012.12.007.

[15] Y. Liu, X. Ge, J. Li, Graphene lubrication, Appl. Mater. Today 20 (2020) 100662, https://doi.org/10.1016/j.apmt.2020.100662.

[16] A.J. Marsden, M. Phillips, N.R. Wilson, Friction force microscopy: a simple technique for identifying graphene on rough substrates and mapping the orientation of graphene grains on copper, Nanotechnology 24 (25) (2013), https://doi.org/10.1088/0957-4484/24/25/255704.

[17] U. Narula, C.M. Tan, C.S. Lai, Growth mechanism for low temperature PVD graphene synthesis on copper using amorphous carbon, Sci. Rep. 7 (2017) 44112, https://doi.org/10.1038/srep44112.

[18] P. Panjan, M. Čekada, M. Panjan, D. Kek-Merl, Growth defects in PVD hard coatings, Vacuum 84 (1) (2009) 209–214, https://doi.org/10.1016/j.vacuum.2009.05.018.

[19] A. Reina, X. Jia, J. Ho, D. Nezich, H. Son, V. Bulovic, M.S. Dresselhaus, K. Jing, Large area, few-layer graphene films on arbitrary substrates by chemical vapor deposition, Nano Lett. 9 (1) (2009) 30–35, https://doi.org/10.1021/nl801827v.

[20] D.T. Oldfield, D.G. McCulloch, C.P. Huynh, K. Sears, S.C. Hawkins, Multilayered graphene films prepared at moderate temperatures using energetic physical vapour deposition, Carbon N Y 94 (2015) 378–385, https://doi.org/10.1016/j.carbon.2015.06.071.

[21] A.C. Ferrari, J. Robertson, Interpretation of Raman spectra of disordered and amorphous carbon, Phys. Rev. B 61 (2000) 14095–14107, https://doi.org/10.1103/PhysRevB.61.14095.

[22] C.V. Thompson, Solid-state dewetting of thin films, Annu. Rev. Mater. Res. 42 (2012) 399–434, https://doi.org/10.1146/annurev-matsci-070511-155048.

[23] Y. Bleu, F. Bourquard, J.-Y. Michalon, Y. Lefkir, S. Reynaud, A.-S. Loir, V. Barnier, F. Garrelie, C. Donnet. Transfer-free graphene synthesis by nickel catalyst dewetting using rapid thermal annealing 555 (2021) 149492. https://doi.org/10.1016/j.apsusc.2021.149492.

[24] J. Su, J. Zhang, Y. Liu, et al., Parameter-dependent oxidation of physically sputtered Cu and the related fabrication of Cu-based semiconductor films with metallic resistivity, Sci. China Mater. 59 (2016) 144–150, https://doi.org/10.1007/s40843-016-0125-y.

[25] H. Ji, Y. Hao, Y. Ren, M. Charlton, W.H. Lee, Q. Wu, H. Li, Y. Zhu, Y. Wu, R. Piner, R.S. Ruoff, Graphene growth using a solid carbon feedstock and hydrogen, ACS Nano 5 (9) (2011) 7656–7661, https://doi.org/10.1021/nn202802x.

[26] F.T. Si, X.W. Zhang, X. Liu, Z.G. Yin, S.G. Zhang, H.L. Gao, J.J. Dong, Effects of ambient conditions on the quality of graphene synthesized by chemical vapor deposition, Vacuum 86 (2012) 1867–1870, https://doi.org/10.1016/j.vacuum.2012.04.035.

[27] G. Bener, V. Kopustinskas, A. Guobienė, Š. Meškinis, A. Vasiliauskas, M. Andrulevičius, Cobalt-activated transfer-free synthesis of the graphene on Si (100) by anode layer ion source, Processes 10 (2) (2022), https://doi.org/10.3390/pr10020272.

[28] C.M. Orofeo, H. Ago, B. Hu, M. Tsuji, Synthesis of large area, homogeneous, single layer graphene films by annealing amorphous carbon on Co and Ni, Nano Res. 4 (6) (2011) 531–540, https://doi.org/10.1007/s12274-011-0109-x.

[29] M. Pan, C. Wang, H.F. Li, N. Xie, P. Wu, X.D. Wang, Z. Zeng, S. Deng, G.P. Dai, Growth of U-shaped graphene domains on copper foil by chemical vapor deposition, Mater. (Basel) 12 (12) (2019) 1887, https://doi.org/10.3390/ma12121887.

[30] S. Nie, J.M. Wofford, N.C. Bartelt, O.D. Dubon, K.F. McCarty, Origin of the mosaicity in graphene grown on Cu(111), Phys. Rev. B - Condens. Matter Mater. Phys. 84 (15) (2011), https://doi.org/10.1103/PhysRevB.84.155425.

[31] J. Li, X. Ge, J. Luo, Random occurrence of macroscale superlubricity of graphite enabled by tribo-transfer of multilayer graphene nanoflakes, Carbon N Y 138 (2018) 154–160, https://doi.org/10.1016/j.carbon.2018.06.001.

[32] E. Tomanik, W. Christinelli, R. Souza, V. Oliveira, F. Ferreira, B. Zhmud, Review of graphene-based materials for tribological engineering applications, Eng. 4 (2023) 2764–2811, https://doi.org/10.3390/eng4040157.

[33] D. Berman, A. Erdemir, A.V. Sumant, Graphene: a new emerging lubricant, Mater. Today 17 (1) (2014) 31–42, https://doi.org/10.1016/j.mattod.2013.12.003. Elsevier B.V.

[34] S. Singh, X. Chen, C. Zhang, R.K. Gautam, R. Tyagi, J. Luo, Tribological performance of steel with multi-layer graphene grown by low-pressure chemical vapor deposition, J Tribol 142 (12) (2020) 122101, https://doi.org/10.1115/1.4047458.

[35] L.G. Cancado, A. Jorio, E.H.M. Ferreira, F. Stavale, C.A. Achete, R.B. Capaz, M.V. O. Moutinho, A. Lombardo, T.S. Kulmala, A.C. Ferrari, Quantifying defects in graphene via raman spectroscopy at different excitation energies, Nano Lett. 11 (2011) 3190–3196, https://doi.org/10.1021/nl201432g.

[36] C. Chen, P. Xue, D. Diao, Graphitization vs tribo-oxidation governing friction behaviors of doped graphene nanocrystalline carbon films, Carbon N Y 197 (2022) 435–443, https://doi.org/10.1016/j.carbon.2022.07.001.

[37] W. Song, P. Chen, J. Yan, W. Zhu, H. Ji, The tribological properties of reduced graphene oxide doped by N and B species with different configurations, ACS Appl. Mater. Interfaces 12 (2022) 29737–29746, https://doi.org/10.1021/acsami.0c03467.